Phase-Field-Lattice Boltzmann Method for Dendritic Growth with Melt Flow and Thermosolutal Convection-Diffusion

Nanqiao Wang[1], David Korba[1,2], Zixiang Liu[3], Raj Prabhu[4], Matthew Priddy[1,2], Shengfeng Yang[5], Lei Chen[6], Like Li[1,2,*]

[1] Department of Mechanical Engineering, Mississippi State University, Mississippi State, MS 39762, USA
[2] Center for Advanced Vehicular Systems, Mississippi State University, Mississippi State, MS 39762, USA
[3] Division of Applied Mathematics, Brown University, Providence, RI 02914, USA
[4] Universities Space Research Association, NASA Glenn Research Center, Cleveland, OH 44135, USA
[5] Department of Mechanical and Energy Engineering, Indiana University-Purdue University Indianapolis, Indianapolis, IN 46202, USA
[6] Department of Mechanical Engineering, University of Michigan-Dearborn, Dearborn, MI 48128, USA

* Corresponding author: likeli@me.msstate.edu

Abstract

We propose a new phase-field model formulated within the system of lattice Boltzmann (LB) equation for simulating solidification and dendritic growth with fully coupled melt flow and thermosolutal convection-diffusion. With the evolution of the phase field and the transport phenomena all modeled and integrated within the same LB framework, this method preserves and combines the intrinsic advantages of the phase-field method (PFM) and the lattice Boltzmann method (LBM). Particularly, the present PFM/LBM model has several improved features compared to the existing phase-field models including: (1) a novel multiple-relaxation-time (MRT) LB scheme for the phase-field evolution is proposed to effectively model solidification coupled with melt flow and thermosolutal convection-diffusion with improved numerical stability and accuracy, (2) convenient diffuse interface treatments are implemented for the melt flow and thermosolutal transport which can be applied to the entire domain without tracking the interface, and (3) the evolution of the phase field, flow, concentration, and temperature fields on the level of microscopic distribution functions in the LB schemes is decoupled with a multiple-time-scaling strategy (despite their full physical coupling), thus solidification at high Lewis numbers (ratios of the liquid thermal to solutal diffusivities) can be conveniently modeled. The applicability and accuracy of the present PFM/LBM model is verified with four numerical tests including

This is the author's manuscript of the article published in final edited form as:

Wang, N., Korba, D., Liu, Z., Prabhu, R., Priddy, M. W., Yang, S., Chen, L., & Li, L. (2021). Phase-field-lattice Boltzmann method for dendritic growth with melt flow and thermosolutal convection–diffusion. Computer Methods in Applied Mechanics and Engineering, 385, 114026. https://doi.org/10.1016/j.cma.2021.114026

isothermal, iso-solutal and thermosolutal convection-diffusion problems, where excellent agreement in terms of phase-field and thermosolutal distributions and dendritic tip growth velocity and radius with those reported in the literature is demonstrated. The proposed PFM/LBM model can be an attractive and powerful tool for large-scale dendritic growth simulations given the high scalability of the LBM.
Keywords: Dendritic growth, solidification, phase field, lattice Boltzmann, multiple-relaxation-time.

1. Introduction

Quantification and prediction of the evolution of the microstructure and segregation patterns of solidified pure materials and alloys are of great scientific and technological interest. The dendritic growth during solidification is a complex multiscale phenomenon that involves phase transition, melt flow, heat and solute convection-diffusion that are fully coupled at the evolving liquid-solid interface of complex morphology. In addition to the nature of multiphysics coupling, large transport property ratios are also encountered in the solidification process, for instance, the solutal diffusivity in the liquid state is generally two to four orders of magnitude smaller than the thermal diffusivity, and the solutal diffusivity in the solid state is typically two to four orders of magnitude smaller than that in the liquid [1]. It is also well known that solidification of alloys differs in many respects from solidification of pure substances, e.g., pure metals solidify at their definite melting point temperatures, while most alloys start to solidify at their liquidus temperatures and complete solidification at the solidus temperatures with the latter lower than the former; and undercooling related microstructure can only be produced by thermal means in pure metals, while in alloys it can be produced by changes in both temperature and composition. Direct simulation of solidification and crystal growth on the scale that captures the local liquid-solid interface geometry (sharp interface) has thus experienced only limited progress [1].

The phase-field method (PFM), which employs the concept of a diffuse interface and introduces a phase field variable (with constant values in the bulk phases and varying steeply yet smoothly in the diffuse interface region), has become a widely accepted technique for computational modeling of dendritic growth and interfacial pattern formation. Several detailed reviews on phase-field modeling of dendritic growth can be found in [2–4]. While the present study focuses on solidification modeling, it should be noted that the PFM has broad applications

in modeling and predicting mesoscale morphological and microstructure evolution in materials such as solid-state phase transformations, grain growth and coarsening, domain evolution in thin films [5], morphological evolution of multicomponent vesicles and solving nonlinear high-order PDEs [6–8], among others. In the early works, the PFM was only employed to model solidification controlled by pure diffusion, and the effects of thermal and solutal diffusion were mostly separately studied. The first *coupled* thermosolutal PFM was proposed in [1] where it was also demonstrated that the coupled model can reduce to the isothermal and iso-solutal cases. The effect of fluid flow and melt convection on the crystal growth was well recognized [9–12], but little work was reported mainly due to the lack of effective and reliable coupled models. Beckermann et al. [13] reported the first phase-field simulations including melt convection, in which the mass, momentum, energy, and species conservation equations in the diffuse interface region were formulated based on volume averaging; and a dissipative interfacial stress term (momentum sink) was introduced in the momentum equation to deal with the interaction at the liquid-solid interface. All the conservation equations were solved with traditional computational fluid dynamics (CFD) schemes in [13]. Since then, a great number of publications on PFM modeling of dendritic growth under melt convection has been reported (e.g., [14–18]).

In the CFD and heat and mass transfer communities, the lattice Boltzmann method (LBM) has become a powerful and alternative numerical method for modeling fluid flows and thermal/mass transport problems with complex geometry due to its attractive features including simple algorithm, easy implementation, convenience in boundary and interface treatment, and compatibility with parallel computing [19–27]. It is no surprise that a growing number of publications have focused (e.g., [14,17,28,29]) on coupling the PFM and LBM for dendritic growth simulations. Most of those PFM-LBM models can be considered as *hybrid* models in which finite-difference- or finite-volume-based PFM was applied to simulate the phase field evolution, while the LBM was implemented to model the melt flow and heat and solute transfer. In addition, fully coupled PFM models considering all the effects of melt flow and thermosolutal convection-diffusion in the literature are very rare (e.g., [30]) due to the lack of general, convenient, and efficient numerical schemes.

Recognizing the capabilities and advantages of the LBM, there has been growing interest in constructing LB schemes to solve the governing equation for the phase field [31–33]; as a result, the generic LB algorithm, and thus a single grid system, can be applied to model all the transport

phenomena as well as the phase field evolution. The current work falls into this category. The main attractive features of the proposed PFM/LBM model in this work include: (1) compared to the isothermal PFM models in [14,32,33] and the iso-solutal PFM models in [17,18,28,29,34–36], the present PFM model is formulated to model fully coupled thermosolutal convection-diffusion; (2) compared to the PFM model in [1,31,37–39] for solidification with coupled thermosolutal pure diffusion, the present model also includes melt flow and thermosolutal convection-diffusion; (3) compared to the single-relaxation-time (SRT) based LBM model for solving the phase-field equation in [31,33,34], the present PFM/LBM model employs the multiple-relaxation-time (MRT) based collision operator for both the phase-field evolution and all the other transport equations, considering the improvement in both numerical accuracy and stability of the MRT-LBM models compared to the traditional SRT-LBM models [23–27]; and (4) the multiple-time-scaling strategy proposed in [40] is implemented in the present model so that different time steps can be used in the evolution of the four sets of microscopic distribution functions defined in the LB schemes for the respective phase field, flow field, concentration field and thermal field, thus decoupled relaxation-time coefficients can be selected, and hence a wide range of characteristic parameters encountered in solidification and dendritic growth processes can be effectively simulated. The applicability and accuracy of the present PFM/LBM model is verified with four representative benchmark test cases including both 2D and 3D examples.

This rest of this paper is organized as follows. The governing equations for the phase field, melt flow, concentration (solute) field, and temperature field and their coupling are described in Section 2. The specific LBM-based numerical schemes in the proposed PFM/LBM model for solving those governing equations are presented in Section 3. Model verification and discussion are then detailed in Section 4. And concluding remarks are provided in Section 5. Lastly, the Chapman-Enskog analysis for the MRT-LBM scheme to recover the phase-field evolution equation is presented in Appendix A, and Appendix B briefly explains the algorithms used to compute the dendritic tip growth velocity and radius.

2. Phase-Field Equation and Conservation Equations

2.1 Phase field

In the phase field methods, a continuous dimensionless phase-field variable, ϕ, is defined with $\phi = -1$ in the liquid phase, $\phi = 1$ in the solid phase, and varying smoothly in the diffuse interface

($-1 \le \phi \le 1$). To determine the governing equation for the phase field in thermosolutal convection-diffusion problems, the following dimensionless concentration (also called supersaturation) and temperature (also called undercooling) variables are defined for the entire domain [1,31]

$$U = \frac{\dfrac{2c/c_\infty}{(1+k)-(1-k)\phi} - 1}{1-k}, \tag{1}$$

$$\theta = \frac{T - T_m - mc_\infty}{L_h / C_p}, \tag{2}$$

where c_∞ is the far-field concentration that equals the initial concentration of the alloy, $k = c_s/c_l$ the partition coefficient that relates the compositions of solid and liquid in contact with each other at the interface, T_m the melting temperature, m the slope of the liquidus line in the phase diagram, L_h the latent heat, and C_p the specific heat. Following the formulations in [1,13,17,31–33], the governing equation for ϕ during solidification and dendritic growth can be written as

$$\tau(\mathbf{n}, U)\partial_t \phi = \nabla \cdot \left[W^2(\mathbf{n}) \nabla \phi \right] + W_0^2 \nabla \cdot \mathbf{N} - f'(\phi) - \lambda \left(Mc_\infty U + \theta \right) g'(\phi), \tag{3}$$

where the relaxation time $\tau(\mathbf{n}, U)$ and the anisotropic interface width $W(\mathbf{n}) = W_0 a_s(\mathbf{n})$ are both functions of the local normal vector $\mathbf{n}$ that can be calculated as $\mathbf{n} = -\nabla\phi / |\nabla\phi|$, W_0 is the characteristic width, λ is a dimensionless parameter that controls the coupling between the phase field and the concentration and temperature fields, $f'(\phi)$ and $g'(\phi)$ are interpolating functions associated with the double-well potential and the free energy of the bulk, respectively, with a popular choice of $f'(\phi) = -\phi + \phi^3$, $g'(\phi) = (1-\phi^2)^2$ [17,31], M is the scaled magnitude of the liquidus slope $M = -m(1-k) / \left(L_h / C_p \right)$, and $\mathbf{N}$ is the anisotropic vector defined as

$$\mathbf{N} = |\nabla\phi|^2 a_s(\mathbf{n}) \left[\frac{\partial a_s(\mathbf{n})}{\partial(\partial_x \phi)}, \frac{\partial a_s(\mathbf{n})}{\partial(\partial_y \phi)}, \frac{\partial a_s(\mathbf{n})}{\partial(\partial_z \phi)} \right]^{\mathrm{T}}. \tag{4}$$

In most previous PFM models, τ is considered as a function of $\mathbf{n}$ only [31–34,36], and $\tau(\mathbf{n}) = \tau_0 a_s^2(\mathbf{n})$ was applied with τ_0 a constant and $a_s(\mathbf{n})$ defined as the crystalline anisotropy function [31–33]

$$a_s(\mathbf{n}) = 1 - 3\varepsilon_s + 4\varepsilon_s \sum_{\sigma=x,y,z} n_\sigma^4 = 1 - 3\varepsilon_s + 4\varepsilon_s \sum_{\sigma=x,y,z} (\partial_\sigma \phi)^4 \Big/ |\nabla\phi|^4, \tag{5}$$

where ε_s is the anisotropic strength. As pointed out by Ramirez et al. [1] and later also implemented in [30,37–39], for coupled thermosolutal transport problems, τ should also be dependent on the concentration field, i.e.,

$$\tau(\mathbf{n},U) = \tau_0 a_s^2(\mathbf{n}) F(U), \tag{6a}$$

and

$$F(U) = \frac{1}{Le} + Mc_\infty \left[1 + (1-k)U\right], \tag{6b}$$

where $Le = \alpha/D_l$ is the Lewis number denoting the ratio between the thermal diffusivity α and solutal diffusivity D_l in the liquid phase. This work also implements the generic definition of $\tau(\mathbf{n}, U)$ in Eq. (6) for thermosolutal convection-diffusion problems. It should be noted that most of the previous PFM models for solidification and dendritic growth considered only the effect of heat transfer (i.e., ϕ and θ coupled only, see e.g., [14,32,33]) or solute transfer (i.e., ϕ and U coupled only, e.g., [17,18,28,29,34–36]); fully coupled thermosolutal diffusion (without convection) problems were studied in [1,31,37–39], while the dependence of τ on U was not taken into account in [31]. The present PFM model (details presented in Section 3) is applicable to more general solidification processes involving fully coupled thermosoltual convection-diffusion. It is also worth noting that the present general PFM model reduces to that for (1) ϕ and θ coupled thermal/iso-solutal transport problems with the selection of $Le = 1$, $Mc_\infty = 0$, and (2) ϕ and U coupled solutal/iso-thermal transport problems with $Le \to \infty$, $Mc_\infty = 1-(1-k)\Omega$ and $U = \dfrac{\Omega}{1-(1-k)\Omega}$, where Ω is the imposed solutal "undercooling" relating c_∞ to the equilibrium liquidus concentration at the system temperature c_l^0, i.e.,

$$\Omega = \frac{c_l^0 - c_\infty}{(1-k)c_l^0}, \tag{7}$$

It is clear that for both simplified versions, $\tau(\mathbf{n}, U)$ in Eq. (6) reduces to $\tau(\mathbf{n}) = \tau_0 a_s^2(\mathbf{n})$.

With the above expressions, Eq. (3) can be rewritten in the explicit form as

$$\tau_0 a_s^2(\mathbf{n}) F(U) \partial_t \phi = W_0^2 \nabla \cdot \left[a_s^2(\mathbf{n}) \nabla \phi \right] + W_0^2 \nabla \cdot \mathbf{N} + \left(\phi - \phi^3\right) - \lambda \left(Mc_\infty U + \theta\right)\left(1-\phi^2\right)^2. \tag{8}$$

2.2 Melt flow

The melt is assumed to be incompressible Newtonian fluid and the flow is governed by the continuity and Navier-Stokes equations

$$\nabla \cdot \mathbf{v} = 0\,, \tag{9}$$

$$\partial_t \mathbf{v} + \mathbf{v} \cdot \nabla \mathbf{v} = -\nabla p/\rho + \nu \nabla^2 \mathbf{v}\,, \tag{10}$$

where **v** is the flow velocity, p the pressure, ρ the density, and ν the viscosity. For sharp interfaces, the no-slip boundary condition should be used. For diffuse interfaces, however, a volume-averaged momentum equation can be formulated, as shown in [13] in the diffuse interface domain; and with the introduction of the phase field, convenient boundary schemes can be implemented at the diffuse interface, such as treating the interfacial flow as a flow in a porous medium [33]. In this work, the latter approach is applied and the specific interface treatment for flow simulation will be presented in the context of the PFM/LBM model (see Section 3.2 below).

2.3 Concentration field

The governing equation for the concentration field can be written as [1,17,29,31,38,41]

$$p_\phi \left(\partial_t U + \mathbf{v} \cdot \nabla U\right) = \nabla \cdot \left(D_\phi \nabla U\right) - \nabla \cdot \mathbf{j}_{at} + \frac{1 + (1-k)U}{2} \partial_t \phi - \nabla \cdot \mathbf{J}\,, \tag{11}$$

where $p_\phi = \frac{1+k}{2} - \frac{(1-k)}{2}\phi$, the interpolated diffusivity $D_\phi = D_s \frac{1+\phi}{2} + D_l \frac{1-\phi}{2}$, $\mathbf{j}_{at}$ is the phenomenological anti-trapping current term defined as [31]

$$\mathbf{j}_{at} = -\frac{1}{2\sqrt{2}} W_0 \left[1 + (1-k)U\right] \frac{\partial \phi}{\partial t} \frac{\nabla \phi}{|\nabla \phi|}\,, \tag{12}$$

and **J** is the flux term associated with fluctuation [17]. The third term on the RHS of Eq. (11) is due to the rearrangement of $\partial_t U$ as U is related to ϕ (see Eq. (1)). In this work, the flux **J** is neglected following the setups in [1,31,33,34,42] for direct quantitative comparison with results reported therein. It should be stressed that in this work, the solute diffusion within the solid phase is also taken into account as in [17,29]. This is different from the models in [1,31,38,41] where solute diffusion in the solid was neglected with $D_\phi = D_l \frac{1-\phi}{2}$.

2.4 Temperature field

The governing equation for the dimensionless temperature considering convection is [1,31,33,38,42]

$$\partial_t \theta + \mathbf{v} \cdot \nabla \theta = \alpha \nabla^2 \theta + \frac{1}{2} \partial_t \phi\,, \tag{13}$$

where α is the thermal diffusivity, the last term in Eq. (13) is related to the latent heat of fusion (see Eq. (2)) during phase change, and the coefficient ½ shows up in Eq. (13) since the bounds for the phase field variable are $\phi = \pm 1$.

3. Present Phase-Field/Lattice-Boltzmann Model (PFM/LBM)

3.1 LB scheme for phase field

By treating the phase-field equation as a transient pseudo-convection-diffusion equation with source terms, and following the idea originally demonstrated in [43] for solute and heat transfer in heterogeneous porous median, an LB scheme was proposed in [31,32] for the phase field with a modified single-relaxation-time (SRT, also called BGK [44]) collision operator:

$$a_s^2(\mathbf{n}) g_\alpha\left(\mathbf{x}+\mathbf{e}_\alpha\delta t, t+\delta t\right) = g_\alpha\left(\mathbf{x},t\right) - \left[1-a_s^2(\mathbf{n})\right] g_\alpha\left(\mathbf{x}+\mathbf{e}_\alpha\delta t, t\right)$$

$$-\frac{1}{\tau_\phi\left(\mathbf{x},t\right)}\left[g_\alpha\left(\mathbf{x},t\right) - g_\alpha^{\mathrm{eq}}\left(\mathbf{x},t\right)\right] + \omega_\alpha \delta_t G_\phi\left(\mathbf{x},t\right)/\tau_0 , \tag{14}$$

where $g_\alpha(\mathbf{x}, t) \equiv g(\mathbf{x}, \boldsymbol{\xi}_\alpha, t)$, $\boldsymbol{\xi}$ is the microscopic particle velocity vector in the LB model and it is discretized to a small set of discrete velocities $\{\boldsymbol{\xi}_\alpha | \alpha = 0, 1, \ldots, m-1\}$, $\mathbf{e}_\alpha$ the αth discrete velocity vector, δt the time step, and ω_α the weight coefficient. The distribution function $g_\alpha\left(\mathbf{x}+\mathbf{e}_\alpha\delta t, t\right)$ evaluated at the adjacent nodes is necessary to recover the correct governing equation for ϕ [31,32]. The macroscopic phase-field variable can be obtained from

$$\phi\left(\mathbf{x},t\right) = \sum_{\alpha=0}^{m-1} g_\alpha\left(\mathbf{x},t\right), \tag{15a}$$

and the equilibrium distribution was defined as [31,32]

$$g_\alpha^{\mathrm{eq}}\left(\mathbf{x},t\right) = \omega_\alpha\left[\phi\left(\mathbf{x},t\right) - \frac{1}{\xi}\mathbf{e}_\alpha\cdot\mathbf{N}\frac{W_0^2}{\tau_0}\frac{\delta t}{\delta x}\right], \tag{15b}$$

with ξ a constant related to the lattice structure ($\xi = 1/3$ in D2Q5 and $\xi = 1/4$ in D3Q7 LB models), and the relaxation time coefficient needs to satisfy

$$\tau_\phi\left(\mathbf{x},t\right) = \frac{1}{\xi}a_s^2(\mathbf{n})\frac{W_0^2}{\tau_0}\frac{\delta t}{\delta x^2} + \frac{1}{2}. \tag{16}$$

The BGK-LB scheme in Eq. (14) was also implemented in [33,34], where the authors introduced an "interface advancing velocity" evoked by the interfacial surface energy and it can be expressed as

$$\mathbf{v}_n \equiv -\mathbf{N}\frac{W_0^2}{\tau_0}\frac{\delta t}{\delta x}. \tag{17}$$

It is noted that the 2nd-order terms of $O(\mathbf{v}_n^2)$ were also included in the equilibrium distribution in [33,34] – a practice generally considered necessary for modeling fluid flow but not for scalar convection-diffusion [24,27].

Based on the modified BGK scheme in Eq. (14) and the discussion in [43] regarding the numerical stability of the modified LB scheme, we present an improved PFM/LBM model in this work for the phase field coupled with thermosolutal convection-diffusion.

First, the phase-field governing equation in (8) is rewritten as

$$\tau_0 a_s^2(\mathbf{n})\partial_t\phi = W_0^2\nabla\cdot\left[\frac{a_s^2(\mathbf{n})}{F(U)}\nabla\phi\right] + W_0^2\nabla\cdot\frac{\mathbf{N}}{F(U)} + \frac{G_\phi}{F(U)}, \tag{18}$$

where $G_\phi = \left(\phi-\phi^3\right) - \lambda\left(Mc_\infty U+\theta\right)\left(1-\phi^2\right)^2$. Clearly, in obtaining Eq. (18), the assumption of "semi-explicit" coupling was applied, i.e., the coupling of U into the phase-field is mainly through the last source term in Eq. (8), while its coupling in the remaining transient, diffusion and pseudo-convection terms in Eq. (8) is assumed to be weak so that $1/F(U)$ was directly moved into the divergence terms. Such an assumption is acceptable for LB simulations with small enough time steps as demonstrated in Section 4 with numerical examples. For problems with strong coupling between U and ϕ, the present model can still be applicable, one just needs to add those originally neglected terms (related to ∇U) to the combined source term.

The present LB evolution scheme is written as

$$\begin{aligned} a_s^2(\mathbf{n})g_\alpha\left(\mathbf{x}+\mathbf{e}_\alpha\delta t, t+\delta t\right) &= g_\alpha\left(\mathbf{x},t\right) - \left[1-a_s^2(\mathbf{n})\right]g_\alpha\left(\mathbf{x}+\mathbf{e}_\alpha\delta t,t\right) \\ &-\mathbf{M}^{-1}\mathbf{S}\left[\mathbf{m}\left(\mathbf{x},t\right)-\mathbf{m}^{\mathrm{eq}}\left(\mathbf{x},t\right)\right]_\alpha + \omega_\alpha\delta t\frac{G_\phi\left(\mathbf{x},t\right)}{F(U)\tau_0}, \end{aligned} \tag{19}$$

where $\mathbf{M}$ is a transformation matrix to map the distribution functions to the moment space through $\mathbf{m} = \mathbf{M}\cdot\mathbf{g}$ and $\mathbf{m}^{\mathrm{eq}} = \mathbf{M}\cdot\mathbf{g}^{\mathrm{eq}}$, and $\mathbf{S}$ is related to the matrix of relaxation time coefficients with the multiple-relaxation-time (MRT) collision operator applied in Eq. (19). We choose the matrices as in [24] and the equilibrium moments can be explicitly obtained as in [25,27]. Specifically, for the D2Q5 MRT-LB model

$$\mathbf{M}=\begin{bmatrix}1 & 1 & 1 & 1 & 1\\ 0 & 1 & -1 & 0 & 0\\ 0 & 0 & 0 & 1 & -1\\ 4 & -1 & -1 & -1 & -1\\ 0 & 1 & 1 & -1 & -1\end{bmatrix},\ \mathbf{S}^{-1}=\mathrm{diag}\left(\tau_{00},\tau_{\phi},\tau_{\phi},\tau_{p},\tau_{p}\right),\quad \text{and} \tag{20a}$$

$$\mathbf{m}^{\mathrm{eq}}=\left(\phi,u_{nx},u_{ny},\frac{2}{3}\phi,0\right)^{\mathrm{T}}=\left(\phi,\frac{v_{nx}}{F(U)},\frac{v_{ny}}{F(U)},\frac{2}{3}\phi,0\right)^{\mathrm{T}},\ \text{in D2Q5,} \tag{20b}$$

while for the D3Q7 MRT-LB model, the following can be similarly obtained

$$\mathbf{M}=\begin{bmatrix}1 & 1 & 1 & 1 & 1 & 1 & 1\\ 0 & 1 & -1 & 0 & 0 & 0 & 0\\ 0 & 0 & 0 & 1 & -1 & 0 & 0\\ 0 & 0 & 0 & 0 & 0 & 1 & -1\\ 6 & -1 & -1 & -1 & -1 & -1 & -1\\ 0 & 2 & 2 & -1 & -1 & -1 & -1\\ 0 & 0 & 0 & 1 & 1 & -1 & -1\end{bmatrix},\ \mathbf{S}^{-1}=\mathrm{diag}\left(\tau_{00},\tau_{\phi},\tau_{\phi},\tau_{\phi},\tau_{p},\tau_{p},\tau_{p}\right),\ \text{and} \tag{21a}$$

$$\mathbf{m}^{\mathrm{eq}}=\left(\phi,u_{nx},u_{ny},u_{nz},\frac{3}{4}\phi,0,0\right)^{\mathrm{T}}=\left(\phi,\frac{v_{nx}}{F(U)},\frac{v_{ny}}{F(U)},\frac{v_{nz}}{F(U)},\frac{3}{4}\phi,0,0\right)^{\mathrm{T}},\ \text{in D3Q7.} \tag{21b}$$

Remark 1. It should be emphasized that in deriving $\mathbf{m}^{\mathrm{eq}}$ in Eqs. (20b, 21b), the equilibrium distribution function is rescaled in the present model as

$$\begin{aligned} g_{\alpha}^{\mathrm{eq}}\left(\mathbf{x},t\right)&=\omega_{\alpha}\left[\phi\left(\mathbf{x},t\right)+\frac{1}{\xi}\mathbf{e}_{\alpha}\cdot\mathbf{u}_{n}\right]=\omega_{\alpha}\left[\phi\left(\mathbf{x},t\right)+\frac{1}{\xi}\mathbf{e}_{\alpha}\cdot\frac{\mathbf{v}_{n}}{F(U)}\right]\\ &=\omega_{\alpha}\left[\phi\left(\mathbf{x},t\right)-\frac{1}{\xi}\mathbf{e}_{\alpha}\cdot\mathbf{N}\frac{W_{0}^{2}}{F(U)\tau_{0}}\frac{\delta t}{\delta x}\right], \end{aligned} \tag{22}$$

where $\mathbf{u}_{n}\equiv\dfrac{\mathbf{v}_{n}}{F(U)}$ with $\mathbf{v}_{n}$ defined in Eq. (17). Additionally, in the relaxation matrices in Eqs. (20a, 21a), the relaxation coefficient τ_{ϕ} related to the diffusion coefficient also needs rescaling to satisfy the following

$$\tau_{\phi}\left(\mathbf{x},t\right)=\frac{1}{\xi}\frac{a_{s}^{2}(\mathbf{n})}{F(U)}\frac{W_{0}^{2}}{\tau_{0}}\frac{\delta t}{\delta x^{2}}+\frac{1}{2}. \tag{23}$$

The other relaxation coefficients do not affect the leading-order numerical solutions and thus $\tau_{00} = \tau_P = 1$ is used for consistency [25–27].

Remark 2. The proposed MRT-LB model for the phase field evolution is able to significantly improve the numerical stability with two combined features. First, it is well known that the LB models with an MRT collision operator generally have better numerical accuracy and stability compared to those with the BGK operator in both fluid flow and scalar transport simulations [22,24,27,45,46]. Therefore, the present MRT-LB scheme in Eq. (19) is considered an improvement from the BGK-LB scheme in Eq. (14). Second, the rearrangement of the governing equation in Eq. (18) and the rescaling of the corresponding equilibria, relaxation coefficients and source term (see Eqs. (19, 20b, 21b, 22, 23)) are crucial in ensuring the numerical stability especially for high Lewis number (*Le*) problems. While one could keep the original governing equation in (8), combine $F(U)$ with $a_s^2(\mathbf{n})$, and construct similar LB scheme as in Eq. (14) such as

$$a_s^2(\mathbf{n})F(U)g_\alpha\left(\mathbf{x}+\mathbf{e}_\alpha\delta_t,t+\delta_t\right)=g_\alpha\left(\mathbf{x},t\right)-\left[1-a_s^2(\mathbf{n})F(U)\right]g_\alpha\left(\mathbf{x}+\mathbf{e}_\alpha\delta_t,t\right)$$
$$-\frac{1}{\tau_\phi\left(\mathbf{x},t\right)}\left[g_\alpha\left(\mathbf{x},t\right)-g_\alpha^{\mathrm{eq}}\left(\mathbf{x},t\right)\right]+\omega_\alpha\delta_t\,G_\phi\left(\mathbf{x},t\right)/\tau_0\,, \tag{24}$$

in Eq. (24) no rescaling is needed for g_α^{eq}, τ_ϕ or G_ϕ, and it can be verified to recover Eq. (8) up to 2nd-order accuracy; the LB scheme in Eq. (24) would become unstable when the magnitude of $F(U)$ is small (noting that $a_s^2(\mathbf{n})$ is of $O(1)$ and $F(U) \sim 1/Le$ in Eq. (6b)) since the RHS of Eq. (24) will be divided by $a_s^2(\mathbf{n})F(U)$ when updating $g_\alpha\left(\mathbf{x}+\mathbf{e}_\alpha\delta_t,t+\delta_t\right)$. This phenomenon was also reported in detail in [43] for low-porosity simulations. Furthermore, it should be noted that as pointed out in [1], in typical solidification of alloys the solutal diffusivity in the liquid state is generally much smaller than the thermal diffusivity (i.e., $Le = \alpha/D >> 1$). Thus small $F(U)$ is encountered in typical alloy solidification processes. Overall, the present PFM/LBM model is well-poised to simulate solidification and dendritic growth with both high- and low-Lewis numbers with improved numerical stability compared to those previous PFM-LBM models.

Remark 3. Accurate and efficient computation of the gradient $\nabla\phi$ is essential in the PFM as it shows up in several different terms (e.g., the normal vector $\mathbf{n}=-\nabla\phi/|\nabla\phi|$, the anisotropy function $a_s(\mathbf{n})$ in Eq. (5), and the anisotropic vector $\mathbf{N}$ in Eq. (4)). As demonstrated in [27,47], in

the LB framework, the scalar gradient can be conveniently computed from the distribution functions. Using the notations in this work, the scheme becomes

$$\frac{\partial \phi}{\partial x_i} = -\frac{1}{\xi \tau_\phi \delta x} \sum_{\alpha=1}^{m-1} e_{\alpha i} g_\alpha^{\mathrm{neq}}, \tag{25}$$

where $g_\alpha^{\mathrm{neq}} = g_\alpha - g_\alpha^{\mathrm{eq}}$ is the non-equilibrium component of the distribution function. It is emphasized that Eq. (25) is a local scheme, i.e., it requires only the populations at the local lattice node and is thus more efficient than using finite-difference schemes that were used in previous PFM models. The second-order accuracy of the scheme in Eq. (25) has been verified in [27,47].

The Chapman-Enskog analysis for the LB evolution equation (19) to recover the phase-field governing equation (18) is presented in Appendix A.

For efficient computation and storage, the LB evolution equation (19) is solved in two steps:

collision step:

$$\hat{g}_\alpha(\mathbf{x},t) = \frac{1}{a_s^2(\mathbf{n})}\Big\{ g_\alpha(\mathbf{x},t) - \left[1 - a_s^2(\mathbf{n})\right] g_\alpha(\mathbf{x}+\mathbf{e}_\alpha \delta t, t) - \left[\mathbf{M}^{-1}\mathbf{S}\cdot\left(\mathbf{m}-\mathbf{m}^{\mathrm{eq}}\right)(\mathbf{x},t)\right]_\alpha + \omega_\alpha \delta t \frac{G_\phi(\mathbf{x},t)}{F(U)\tau_0}\Big\}, \text{ and} \tag{26a}$$

streaming step:

$$g_\alpha(\mathbf{x}+\mathbf{e}_\alpha \delta t, t+\delta t) = \hat{g}_\alpha(\mathbf{x},t), \tag{26b}$$

where $\hat{g}_\alpha$ represents the post-collision state.

3.2 LB scheme for melt flow

The incompressible melt flow in the liquid phase can be simulated with the widely used D3Q19 and D2Q9 MRT-LB models [45,46]. In the diffuse interface, the flow can be considered as porous medium flow. To avoid tracking the sharp interface with no-slip boundary condition, we adopt the gray LB scheme [48–50] for porous medium flows to handle the diffuse interface. The collision-streaming procedure for melt flow becomes

collision step:

$$\hat{f}_\alpha(\mathbf{x},t) = f_\alpha(\mathbf{x},t) - \left[\mathbf{M}^{-1}\mathbf{S}\cdot\left(\mathbf{m}-\mathbf{m}^{\mathrm{eq}}\right)(\mathbf{x},t)\right]_\alpha, \text{ and} \tag{27a}$$

streaming step:

$$f_\alpha\left(\mathbf{x}+\mathbf{e}_\alpha\delta_t,t+\delta_t\right)=\hat{f}_\alpha\left(\mathbf{x},t\right)+\theta_f\left(\mathbf{x}+\frac{1}{2}\mathbf{e}_\alpha\delta_t,t\right)\left[\hat{f}_{\bar{\alpha}}\left(\mathbf{x}+\mathbf{e}_\alpha\delta_t,t\right)-\hat{f}_\alpha\left(\mathbf{x},t\right)\right], \quad (27b)$$

where the details of the matrices **M**, **S** and the equilibrium moments $\mathbf{m}^{eq}$ can be found in [45,46] and are not shown here for brevity, and the subscript $\bar{\alpha}$ denotes the opposite direction of α (i.e., $\mathbf{e}_{\bar{\alpha}}=-\mathbf{e}_\alpha$). The fraction coefficient θ_f is related to the solid fraction that can be calculated from the phase-field variable ($\theta_f=(\phi+1)/2$) and is evaluated at the midpoint of the link in Eq. (27b), i.e.,

$$\theta_f\left(\mathbf{x}+\frac{1}{2}\mathbf{e}_\alpha\delta_t,t\right)=\frac{\theta_f\left(\mathbf{x},t\right)+\theta_f\left(\mathbf{x}+\mathbf{e}_\alpha\delta_t,t\right)}{2}=\frac{\phi\left(\mathbf{x},t\right)+\phi\left(\mathbf{x}+\mathbf{e}_\alpha\delta_t,t\right)+2}{4}. \quad (28)$$

The LB scheme for melt flow in Eq. (27) and the calculation of the macroscopic variables including density and velocity are applicable to the entire computational domain under the PFM/LBM framework. Specifically, all the terms in Eq. (27b) are considered within the diffuse interface region; additionally, it reduces to the standard LB scheme for fluid flow within the melt at $\theta_f=(\phi+1)/2=0$, and to the bounce-back scheme which represents the no-slip condition within the solid phase at $\theta_f=1$. Similar discussion was also presented by Sun et al. [33], however, it should be noted that in [33] the pre-collision distribution functions $f_{\bar{\alpha}}\left(\mathbf{x}+\mathbf{e}_\alpha\delta_t,t\right)$ and $f_\alpha\left(\mathbf{x},t\right)$ were used in the last term in Eq. (27b). To correctly recover the governing equations for flow in porous media, post-collision terms as shown in Eq. (27b) should be used. One can refer to [48] for a detailed comparison of the various LB schemes for porous media flow and their Chapman-Enskog analyses.

For dendritic growth modeling with melt flow and dendrite movement under external forces (e.g., gravity or buoyance forces as in [17,35,51]), the body forces can be conveniently added in the LB scheme in Eq. (27) using standard body force treatments in the LB model. Thus the PFM/LBM model is an attractive and powerful tool for large scale simulations of solidification processes with motion of multiple dendrites [35,51].

3.3 LB scheme for concentration field

To apply the LB method to solve for the concentration (supersaturation) field, the governing equation (11) is reorganized to an anisotropic convection-diffusion equation (CDE) with a general source term

$$\partial_t U+\mathbf{v}\cdot\nabla U=\nabla\cdot\left(D_{eff}\nabla U\right)+G_U, \quad (29)$$

where $D_{eff} = \dfrac{D_\phi}{p_\phi} = \dfrac{(1+\phi)D_s + (1-\phi)D_l}{(1+k)-(1-k)\phi}$, and the combined source term becomes

$$G_U = -\frac{(1-k)\left[(1+\phi)D_s + (1-\phi)D_l\right]}{\left[(1+k)-(1-k)\phi\right]^2}\nabla U\cdot\nabla\phi + \frac{\left[1+(1-k)U\right]\partial_t\phi - 2\nabla\cdot\mathbf{j}_{at}}{(1+k)-(1-k)\phi}. \tag{30}$$

It is noted that $\nabla\left(p_\phi^{-1}\right) = \dfrac{2(1-k)}{\left[(1+k)-(1-k)\phi\right]^2}\nabla\phi$ was used in deriving Eq. (30). In this work, the CDE in (29) will be solved with the D2Q5/D3Q7 MRT-LB models [24,27]. By introducing the set of distribution functions $h_\alpha(\mathbf{x}, t)$, the dimensionless concentration is obtained from $U(\mathbf{x},t) = \sum_{\alpha=0}^{m-1} h_\alpha(\mathbf{x},t)$, and the collision-streaming procedure for the LB evolution equation includes

collision step:

$$\hat{h}_\alpha(\mathbf{x},t) = h_\alpha(\mathbf{x},t) - \left[\mathbf{M}^{-1}\mathbf{S}\cdot\left(\mathbf{m}-\mathbf{m}^{\mathrm{eq}}\right)(\mathbf{x},t)\right]_\alpha + \omega_\alpha\delta t G_U(\mathbf{x},t), \text{ and} \tag{31a}$$

streaming step:

$$h_\alpha\left(\mathbf{x}+\mathbf{e}_\alpha\delta t, t+\delta t\right) = \hat{h}_\alpha(\mathbf{x},t). \tag{31b}$$

The matrices **M** and **S** are the same as those in Section 3.1 and the details of equilibrium moment $\mathbf{m}^{\mathrm{eq}}$ can be found in [24,27]. It is worth noting that the principal relaxation time coefficients are related to the effective diffusion coefficient through $\tau_U = 3D_{eff} + 0.5$. With the MRT collision operator implemented, the present LB model is stable in handling solutal convection-diffusion with very large diffusivity ratios. Numerical verification with $D_l/D_s = 10^4$ will be presented in Section 4.3. Some additional remarks are given below.

First, the present LB model for solute convection-diffusion is considered much more convenient and easier to implement than the LB model proposed in [31], where $D_{eff} = \dfrac{(1-\phi)D_l}{(1+k)-(1-k)\phi}$ was assumed neglecting diffusion in the solid phase. As a consequence, in order to apply the LB model to the entire domain for U evolution, the relaxation coefficient τ_U was chosen to be related to the D_l even within the solid phase; and additional rearrangement of the governing equation for U as well as redefinition of the equilibrium distribution function were used in [31]. The present LB model avoids those complex steps and is able to model diffusion within the solid as well.

Second, similar to computing $\nabla\phi$ in the LB model, the gradient ∇U is also conveniently obtained from a local scheme similar to that in Eq. (25) based on the distribution functions in the LB model. It is also noted that, however, for computing $\nabla\cdot\mathbf{j}_{at}$ in Eq. (30), one has to adopt conventional schemes (the central-difference scheme is applied in this work) as in all previous PFM models. And the simple forward Euler method, $\partial_t\phi=\dfrac{\phi(\mathbf{x},t)-\phi(\mathbf{x},t-\delta t)}{\delta t}$, is used for computing $\partial_t\phi$ in the combined source term in Eq. (30).

3.4 LB scheme for temperature field

The energy equation (13) can also be considered as a standard CDE with a source term ($G_\theta=\dfrac{1}{2}\partial_t\phi$) and the above D2Q5/D3Q7 MRT-LB models [24,27] will also be implemented for the temperature field evolution. For completeness, the collision-streaming procedure is also shown below where $n_\alpha(\mathbf{x}, t)$ is the last set of distribution function defined to yield $\theta(\mathbf{x},t)=\sum_{\alpha=0}^{m-1}n_\alpha(\mathbf{x},t)$

collision step:

$$\hat{n}_\alpha(\mathbf{x},t)=n_\alpha(\mathbf{x},t)-\left[\mathbf{M}^{-1}\mathbf{S}\cdot\left(\mathbf{m}-\mathbf{m}^{\mathrm{eq}}\right)(\mathbf{x},t)\right]_\alpha+\omega_\alpha\delta t G_\theta(\mathbf{x},t),\ \text{and} \tag{32a}$$

streaming step:

$$n_\alpha\left(\mathbf{x}+\mathbf{e}_\alpha\delta t,t+\delta t\right)=\hat{n}_\alpha(\mathbf{x},t). \tag{32b}$$

The flow chart for the present PFM/LBM model for solidification and dendritic growth simulation with fully coupled melt flow and thermosolutal convection-diffusion is depicted in Fig. 1.

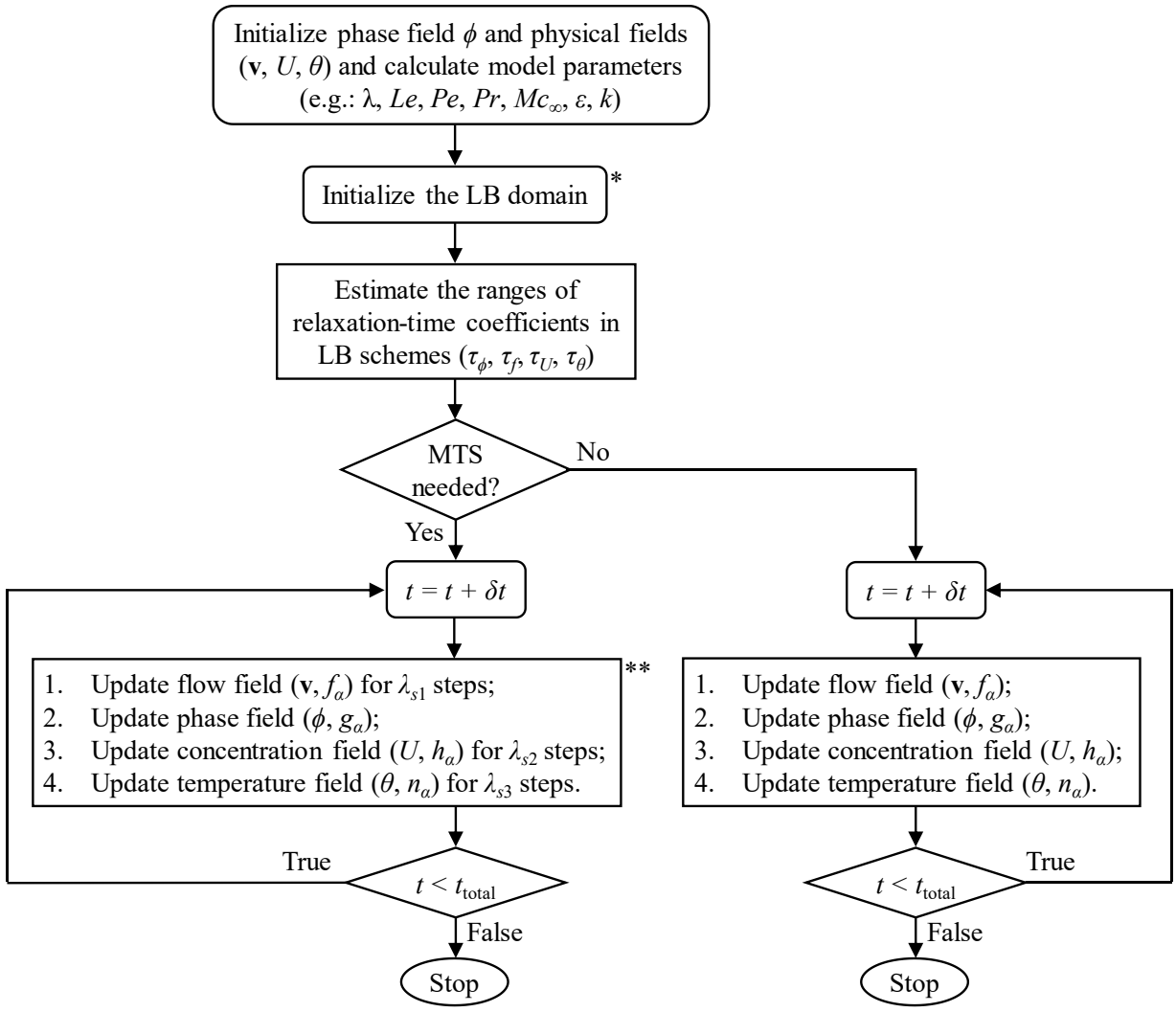

* Converged flow and DFs f_α for flow over the initial seeds can be used;
** Scaling factors λ_{s1}, λ_{s2}, and λ_{s3} can be chosen independently with the MTS used for each LB scheme.

Fig. 1. Flow chart for the proposed fully coupled PFM/LBM model. Here MTS represents the multiple-time-scaling (MTS) strategy developed in [40]**.**

4. Numerical Verification and Discussion

In this section, we implement the present PFM/LBM model to simulate four representative solidification problems with coupled melt flow and thermosolutal convection-diffusion. The applicability and accuracy of the proposed model is verified through detailed comparison of the simulated results with published data in the literature. In each test, a single circular/spherical solid seed of radius R_s is initially placed in the center of a 2D/3D domain with an initial phase-field distribution $\phi_0 = \tanh\left[\left(R_s - d_s\right)/\sqrt{2W_o}\right]$, where d_s is the distance from the seed center;

solidification and dendritic grow under various melt flow, heat, and solute transport conditions are simulated. Specifically, the first test focuses on iso-solutal solidification in 2D with the coupled melt flow, phase field, and temperature field evolution simulated; the second test is for isothermal solidification in 2D; fully coupled thermosolutal convection-diffusion in 2D is simulated in the third test; and 3D simulations are presented in the fourth test. The evolution of the phase field, melt flow, concentration (supersaturation) and temperature fields is checked for each case, and quantitative verification of the simulated results in terms of tip velocity and radius, and selected concentration/temperature profiles is presented. The details for accurate computation of the tip velocity and radius based on the solved phase field are given in Appendix B.

4.1 Thermal/iso-solutal dendritic solidification in 2D

The 2D computational domain is shown in Fig. 2, where the domain size is set as a square with $512\delta x \times 512\delta x$ grid resolution and the initial seed radius is $R_s = 10\delta x$. The characteristic parameters for convection-diffusion are $Pe_\alpha = \frac{W_0^2}{\alpha \tau_0} = 0.25$ and $Pr = \nu/\alpha = 23.1$, and the inlet velocity is set as $u_{in} = W_0/\tau_0$ for convection and $u_{in} = 0$ for pure diffusion problems. The length and time scales are controlled by selected interface thickness $W_0 = 2.5\delta x$ and reference time $\tau_0 = 125\delta t$ with unit spatial and time steps (δx = δt = 1) in the LB framework. To simulate the coupled thermal/iso-solutal solidification and be consistent with reported simulations in the literature, the parameters in the PFM model are chosen as Le = 1, $Mc_\infty = 0$, $\varepsilon_s = 0.05$ and $\lambda = a_1 W_0/d_0 = 6.3826$ with constant $a_1 = 0.8839$. Under the above parameter settings, the relaxation coefficient in the thermal LB model is $\tau_g = 1.1$ which results in $\tau_{f,\text{original}} = 14.36$ in the hydrodynamic LB model if the same time scaling is utilized. Such a large relaxation coefficient would lead to instability of the model and/or large numerical error. Therefore, we implement the multiple-time-scaling (MTS) strategy in [40] and decouple the time steps in the LB models. The effect of this scaling factor, $\lambda_s = \frac{\tau_{f,\text{original}} - 0.5}{\tau_{f,\text{scaled}} - 0.5}$, is studied in Fig. 11 below, and for all the other results presented λ_s = 15 was used, which would render $\tau_{f,\text{scaled}}$ = 1.424.

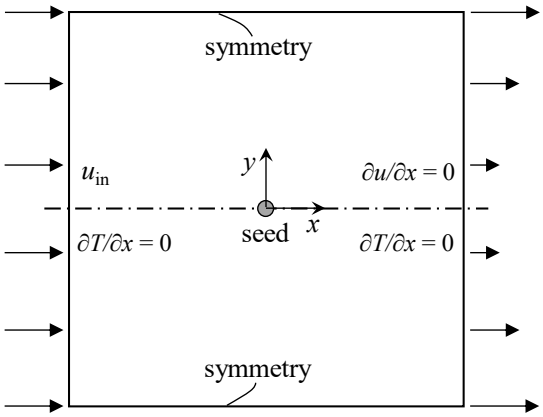

Fig. 2. Schematic depiction of the square computational domain for dendritic growth with melt convection with boundary conditions specified on all four walls and a circular seed located at the center.

Dendritic solidification under pure diffusion is considered first. Fig. 3 shows the phase field interface ($\phi = 0$) at different times with both the BGK- and MRT-LB models for the phase-field evolution implemented (see Sec. 3.1). Excellent agreement between the results from the two LB models in Fig. 3 and also between the present results and those in previous studies [31,33] is observed, confirming the accuracy of the proposed MRT-LB model for the phase field in this work. The results from the MRT-LB model are thus shown throughout this paper. Furthermore, the dimensionless temperature contours and the phase-field "advancing velocity" (see Eq. (17)) components in x- and y-directions are shown in Figs. 4 and 5, respectively, at the time of t/τ_0 = 128.

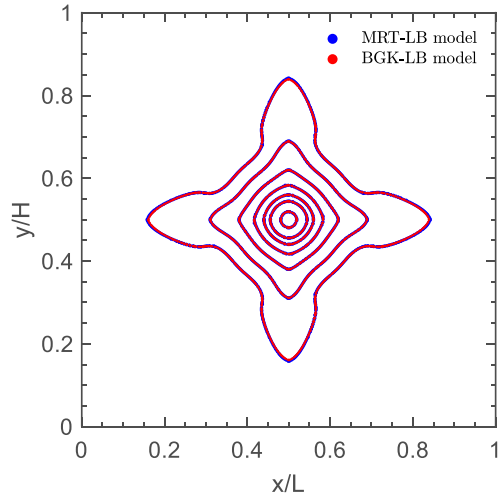

Fig. 3. Interface evolution comparison between the MRT- and BGK-LB models for the phase field for 2D dendritic growth with pure diffusion at t/τ_0 = 0, 4, 8, 16, 32, 64, 128.

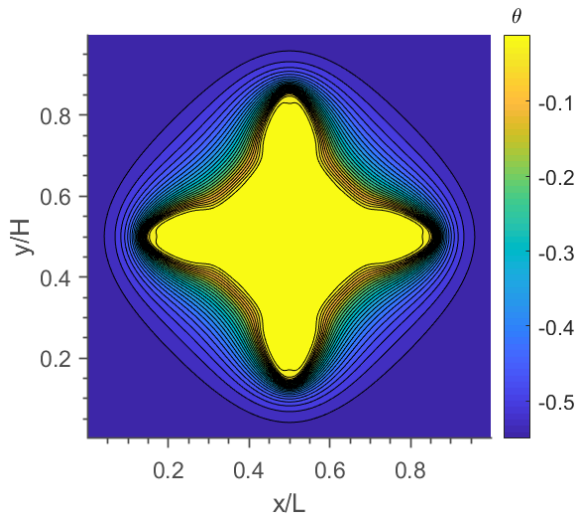

Fig. 4. Contours of the temperature field for 2D dendritic growth with pure diffusion at $t/\tau_0 = 128$.

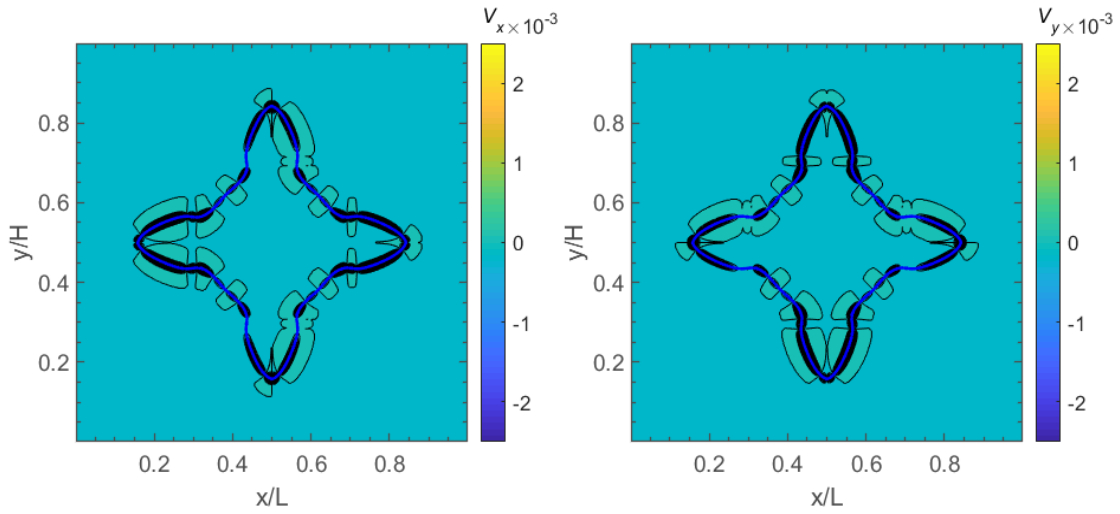

Fig. 5. Interface advancing velocity contours in (a) *x*-direction and (b) *y*-direction for 2D dendritic growth with pure diffusion at $t/\tau_0 = 128$.

The velocity contours in Fig. 5 clearly show that the advancing velocities are much more significant in the diffuse interface region compared to the rest of the domain. It should be noted that the velocity components are evaluated at the LBM nodes with the convenient local scheme in the LBM framework (see Eq. (25)); this allows direct and quantitative investigation of the diffuse interface growth at different locations of interest in addition to the tip velocities that were studied in previous publications. To further verify the present model, Fig. 6 compares the tip velocity and radius results with those reported in [31,33].

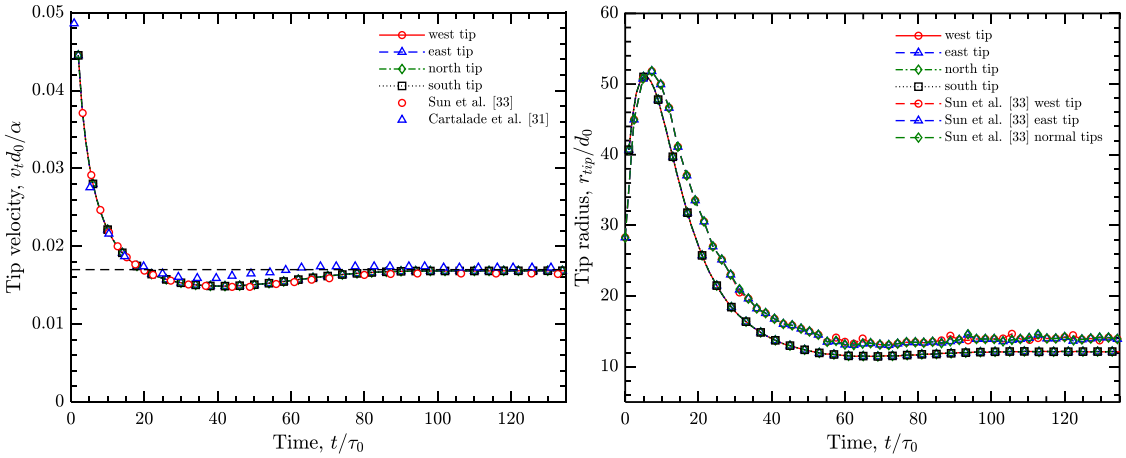

Fig. 6. Evolution of (a) tip velocities, and (b) tip radii for 2D dendritic growth with pure diffusion.

The computed values at the four tips are the same for pure diffusion case, confirming the self-consistence of the model and simulation results. Good agreement for the tip velocity with those in [31,33] and the steady-state analytical value (dashed line) is observed in Fig. 6a; and our simulation shows smoother and more consistent tip radius data in Fig. 6b compared to Sun et al.'s [33], where the tips showed fluctuating results.

Next, we report the simulation results for the 2D dendritic solidification with both thermal convection and diffusion. Fig. 7 shows the interface comparison at the same times as in Fig. 3. It is clearly observed that convection plays a significant role on the dendrite growth, with the west (upstream) tip becoming much larger than the other tips. Consistent results are obtained from both BGK- and MRT-LB models with some discrepancy noticed at the west tip at $t/\tau_0 = 128$. The respective contours of the temperature field and the phase-field advancing velocity components under convection at $t/\tau_0 = 128$ are shown in Figs. 8 and 9, where the effect of thermal convection is obvious compared to those in Figs. 4 and 5. In addition, the evolution of the tip velocities and radii is presented in Fig. 10. The tip velocity comparison further illustrates the significant influence of the fluid flow and thermal convection on the dendrite growth: the upstream west tip has much higher growth velocity and the downstream east tip lower velocity compared to the symmetric north and south tips perpendicular to the inlet flow; and excellent agreement with those reported in [33] is observed. The evolution of the radii of the four tips is close to each other, and also in good agreement with that in [33]. Consistent with the comparison in Fig. 6b, our model and tip radius evaluation scheme (see Appendix B) yield improved results compared to those in [33].

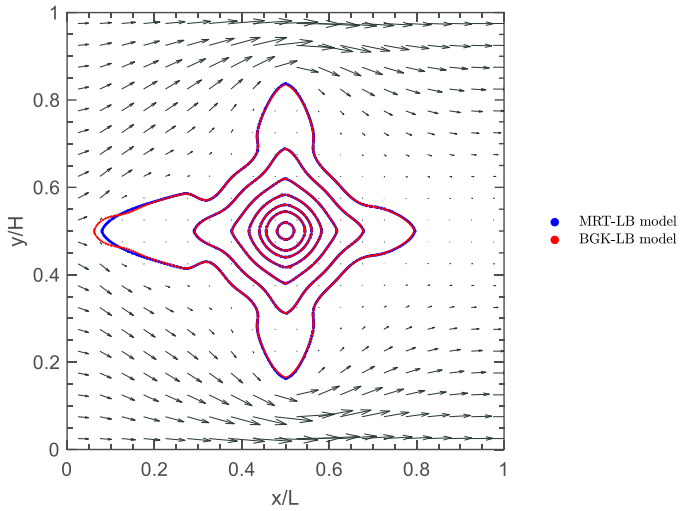

Fig. 7. Interface evolution comparison between the MRT- and BGK-LB models for the phase field for 2D dendritic growth with convection-diffusion at t/τ_0 = 0, 4, 8, 16, 32, 64, 128. The melt flow velocity vectors are shown at t/τ_0 = 128.

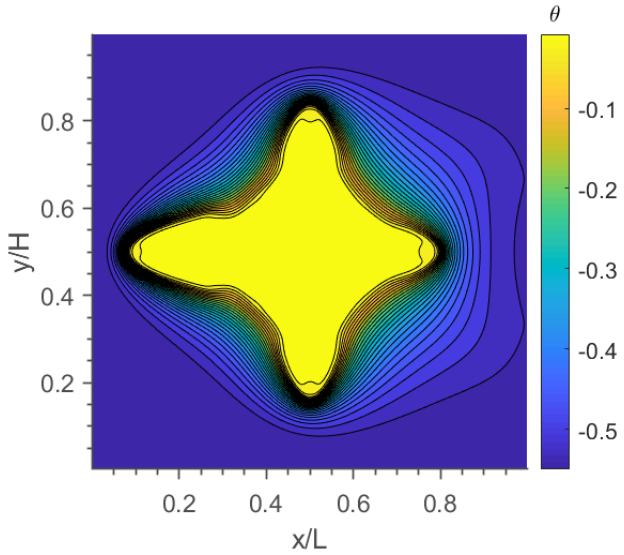

Fig. 8. Contours of temperature field for 2D dendritic growth with convection-diffusion at t/τ_0 = 128.

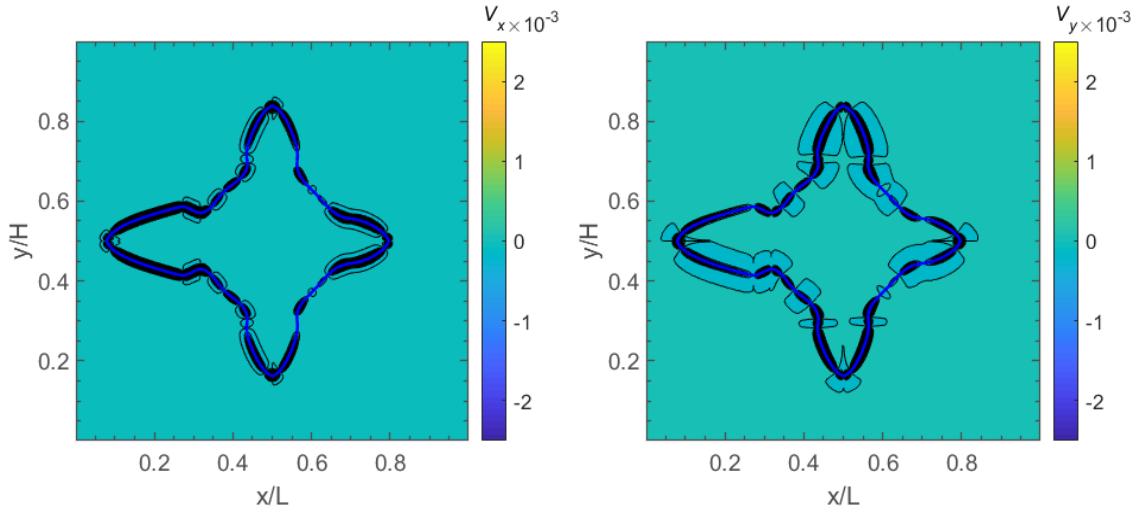

(a) (b)

Fig. 9. Interface advancing velocity contours for 2D dendritic growth with convection-diffusion at $t/\tau_0 = 128$.

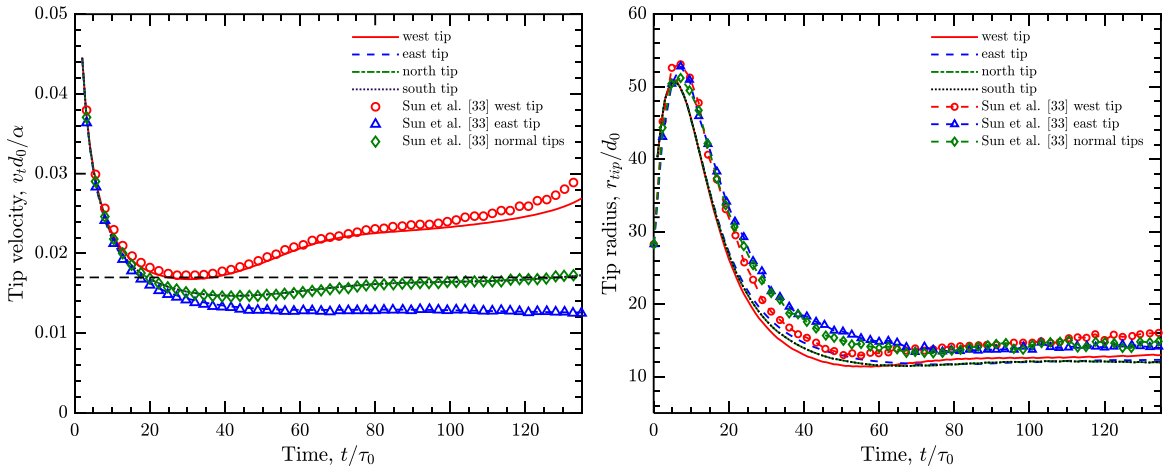

(a) (b)

Fig. 10. Evolution of (a) tip velocities and (b) tip radii for 2D dendritic growth with convection-diffusion.

Furthermore, the efficacy of the multiple-time-scaling (MTS) strategy, which is critical in decoupling the time steps in the different LB schemes in the coupled PFM/LBM model, is demonstrated in Fig. 11, where the comparison of the tip growth velocities and radii at different scaling factor λ_s values is shown. With the selected Prandtl number Pr = 23.1, the rescaled relaxation-time coefficients for the melt flow are $\tau_{f,\text{scaled}}$ = 1.424, 0.962, and 0.731 at λ_s = 15, 30,

and 60, respectively. In general, very good agreement can be observed in both tip velocity and radius results in Fig. 11, confirming the applicability and accuracy of the MTS scheme.

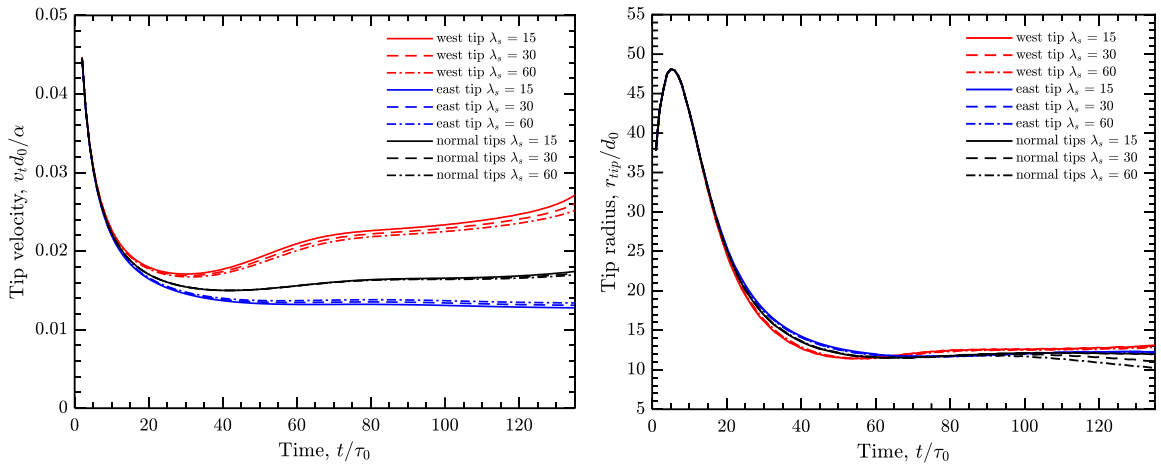

(a) (b)

Fig. 11. Comparison of the (a) tip velocities and (b) tip radii with the multiple-time-scaling (MTS) strategy implemented using various λ_s values for 2D dendritic growth with convection-diffusion.

4.2 Solutal/iso-thermal dendritic solidification in 2D

The 2D MRT-LB schemes for the phase field coupled with the concentration field is verified in this section with the 2D isothermal solidification problem with pure diffusion that has been studied by various authors such as Karma [36] with the finite-difference Euler method, Cartalade et al. [31] using the BGK-LB schemes for both fields, and Wang et al. [34] with a hybrid BGK-LB/finite-volume method for the respective phase field and concentration field. In present simulations, the scaled solute mass diffusivity is selected as $\tilde{D}_l = D_l \tau_0 / W_0^2 = 2$ with interface thickness $W_0 = 2.5\delta x$ and constant time scale $\tau_0 = 50\delta t$. The ratio of the solutal diffusivity in solid to liquid is $D_s / D_l = 10^{-4}$ in all cases considered including the following Section 4.3. Other model parameters include $\lambda = 3.1913$, intial dimensionless cocentration Ω_0 = -0.55 (see Eq. (6)), $\theta = 0$, $k = 0.15$, $\varepsilon_s = 0.02$, and $Mc_\infty = 0.5325$. The computation domian has a $1000\delta x \times 1000\delta x$ uniform mesh and with an initial seed radius $R_s = 10\delta x$.

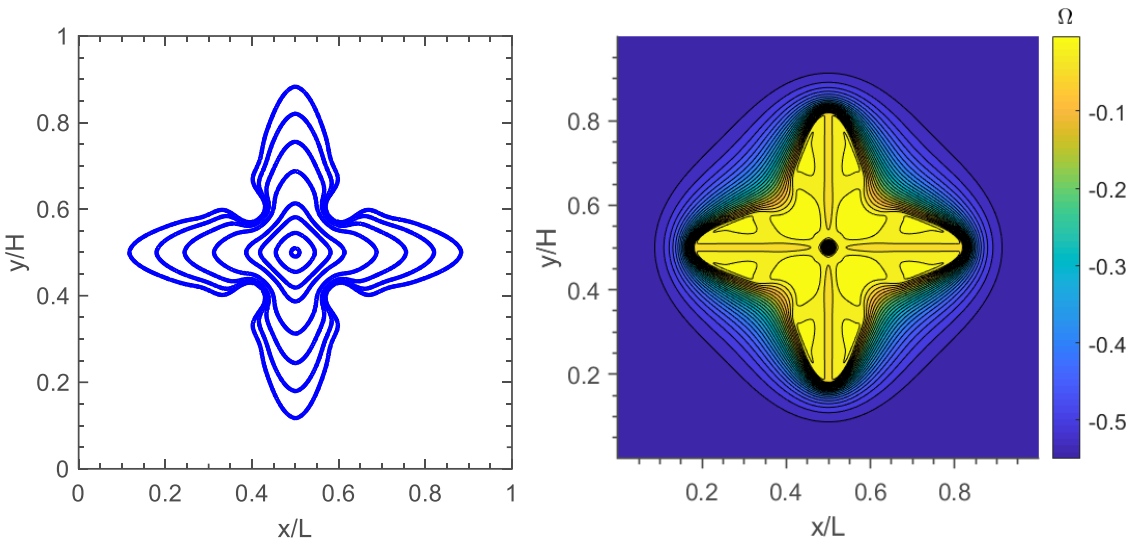

Fig. 12. (a) Phase-field interface evolution at t/τ_0 = 0, 40, 120, 200, 400, 600, 800, and 1000, and (b) concentration field at t/τ_0 = 800 for the 2D dendritic growth with pure diffusion.

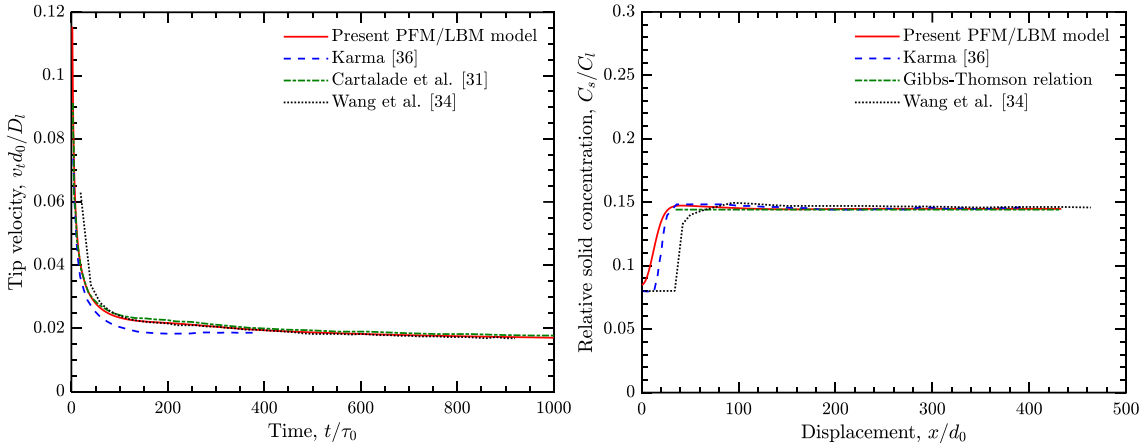

Fig. 13. (a) Dendritic tip velocity variation and (b) concentration profile in the solid phase for the 2D isothermal dendritic growth with solute diffusion.

The interface morphology of ϕ at different times and the distribution of Ω at $t/\tau_0 = 800$ are shown in Fig. 12. The results are consistent with those reported in [1,31,34]. It should be noted that different from the previous models [1,31,34] where $D_l = 0$ was assumed, the present model also considers the solutal transfer within the solid phase ($D_s/D_l = 10^{-4}$), therefore the concentration gradient on the solid side can be clearly observed in Fig. 12(b). To quantify the comparison with published results, Fig. 13(a) shows the variation of simulated tip velocity and Fig. 13(b) the central solute profiles along the y-axis in the solid at $t/\tau_0 = 800$. Due to the symmetry of the pure

diffusion case, we only present the results of the north tip in Fig. 13; and the solute profile obtained from the Gibbs-Thomson relation $C_s / C_l = k[1-(1-k)d_0 / r_{tip}]$, where r_{tip} is the dendritic tip radius (r_{tip} = 21.996δx with the present bi-cubic interpolation used), is also included in Fig. 13(b). Good agreement with published results is observed for both the tip velocity and solute profile in Fig. 13, confirming the accuracy of the present PFM/LBM model for isothermal solidification simulations. The discrepancies in the solute profiles near the dendrite center might be caused by (1) different initial seed radii used in the various simulations (e.g., R_s = 10δx = 14.4d_0 in present simulation, R_s = 22d_0 in [36], and R_s not specified in [34]), and (2) slightly higher relative concentration at the center ($C_s / C_l = 0.085$ in present) than the reference value $C_s / C_l = 0.08$ in [34,36] since the present model considers non-zero diffusity D_s in the solid phase.

4.3 Thermosolutal solidification and dendritic growth in 2D

In this section, the PFM/LBM model is implemented to simulate the 2D dendritic growth of a binary alloy into an undercooled melt with coupled melt flow and thermosolutal convection-diffusion. The diffusion cases at Le = 1 and 50 studied in [1] are used for model verification; and we also report our simulation results under convection at Le = 50.

First, for the diffusion case with Le = 1, the same parameters as in [1] are used including λ = 3.1913, $Mc_\infty = 0.5325$, U_0 = 0, θ_0 = -0.55, k = 0.15, ε_s = 0.02, and $\tilde{D}_l = D_l \tau_0 / W_0^2 = 2$; addtionally, we choose the reference length and time scales $W_0 = 2.5\delta x$ and $\tau_0 = 55\delta t$, respectively, which yield a domain size of 2395δx × 2395δx to maintain the same resolution as in [1]. And the same initial seed radius is also used (R_s = 65d_0 = 45δx). The evolution of the tip velocity and radius (results are symmetric for the four tips) is presented in Fig. 14, where it is clear that the tip velocity matches extremely well with the reference data, and although persistent discrepancy in the tip radius results is noticed at small times, they both converge to close steady results. It is speculated that the initial phase field, $\phi(\mathbf{x},0) = \tanh\left[(R_s - d_s)/\sqrt{2W_o}\right]$ with d_s the distance to the seed center used in the present simulation following [31] could be responsible for the early deviation in Fig. 14(b). To further verify the accuracy of the present model, Fig. 15 shows the comparison of the profiles of ϕ, U, and θ along the central dendrite axis with those in [1] at tD_l / d_0^2 = 470,000. The present results match very well with the published data in general, and the discrepancy in the U

profiles near the dendrite center is due to the non-zero solid solute diffusivity ($D_s / D_l = 10^{-4}$) used, as a similar behavior is also noted in Fig. 13(b).

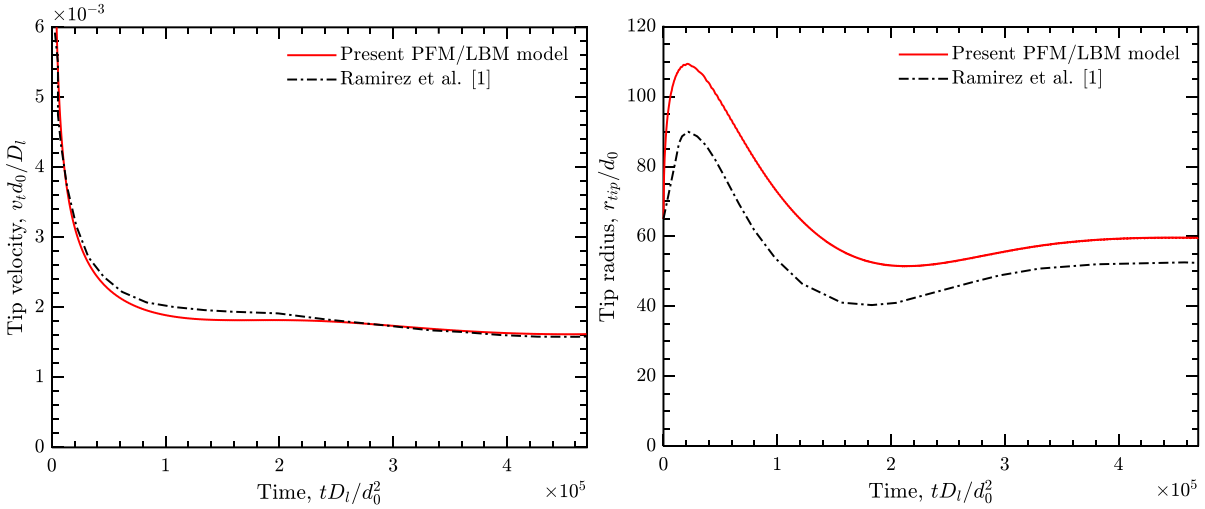

Fig. 14. Evolution of (a) tip velocity and (b) tip radius for the 2D thermosolutal dendritic growth with pure-diffusion at *Le* = 1.

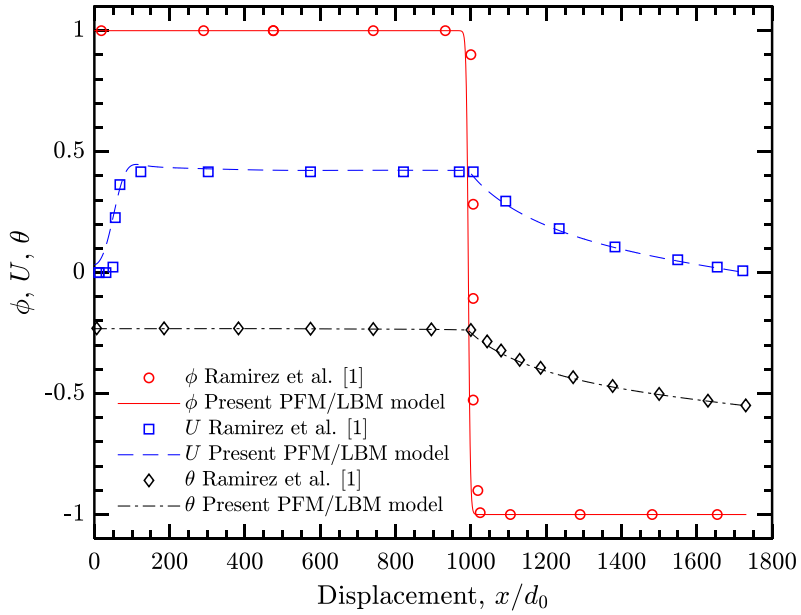

Fig. 15. Simulated ϕ, U, and θ profiles along the central dendrite axis at tD_l/d_0^2 = 470,000.

Next, thermosolutal dendritic growth at higher Lewis numbers is simulated. As emphasized in Section 3.1, the present PFM/LBM model is particularly stable in simulating high *Le* cases. For illustration purposes, Fig. 16 (a-f) presents the phase field, concentration, and temperature fields at tD_l / d_0^2 = 3500 for both the diffusion-only and convection-diffusion cases. The simulation

parameters include Le = 50, λ = 1.5957, $\tilde{D}_l$ = 1, Mc_∞ = 0.1, k = 0.15, ε_s = 0.02, $W_0 = 2\delta x$, and $\tau_0 = 1000\delta t$; initial distributions $\phi_0 = \tanh\left[\left(R_s - d_s\right)/\sqrt{2W_o}\right]$, U_0 = 0, and θ_0 = -0.55 and far-field Dirichlet boundary conditions ϕ = -1, U = 0, and θ = -0.55 are employed; and the computational domian size is $1751\delta x \times 1751\delta x$ with two initial seed radii $R_s = 20\delta x$ and $R_s = 44\delta x$ tested. Similar to the convection test in Section 4.1, constant inlet flow condition ($u_{in} = W_0/\tau_0$) and the converged flow field over the circular seed as initial condition are implemented for the convection-diffusion case with $Pe_\alpha = \frac{W_0^2}{\alpha\tau_0} = \frac{1}{\tilde{D}_l Le} = 0.02$ and Pr = 23.1. The distributions in Fig. 16 are very similar to those reported in [1] for pure diffusion and [30] for convection-diffusion dendritic growth. In particular, the complex microsegregation pattern in the solid is fully captured; the thermal boundary layer thickness is much larger than that of the solutal boundary layer due to the high Le simulated; the concentration variations are mainly confined within the solid phase with more complex contours obtained compared to those in [1] as a non-zero solid solutal diffusivity is used in the present model; noticeable temperature variations in a much larger domain are observed including those in the solid; and the effects of the melt flow and convection on the field distributions are also clearly seen in Fig. 16 (b, d, f) with the upstream primary and secondary tips growing much faster and with significantly higher tip temperature compared to the pure diffusion case in Fig. 16 (a, c, e).

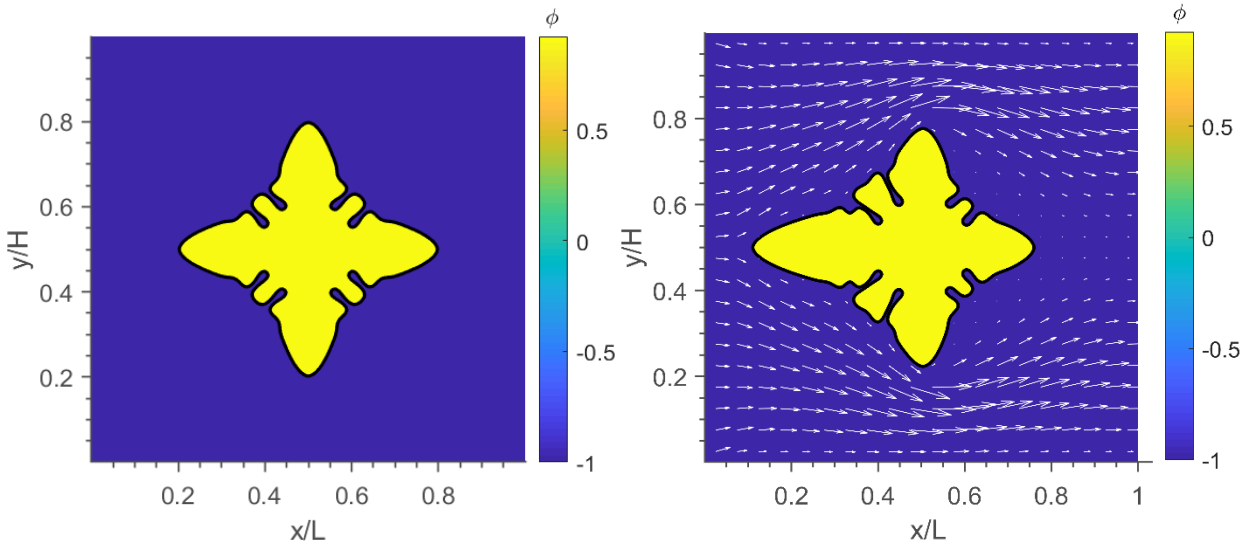

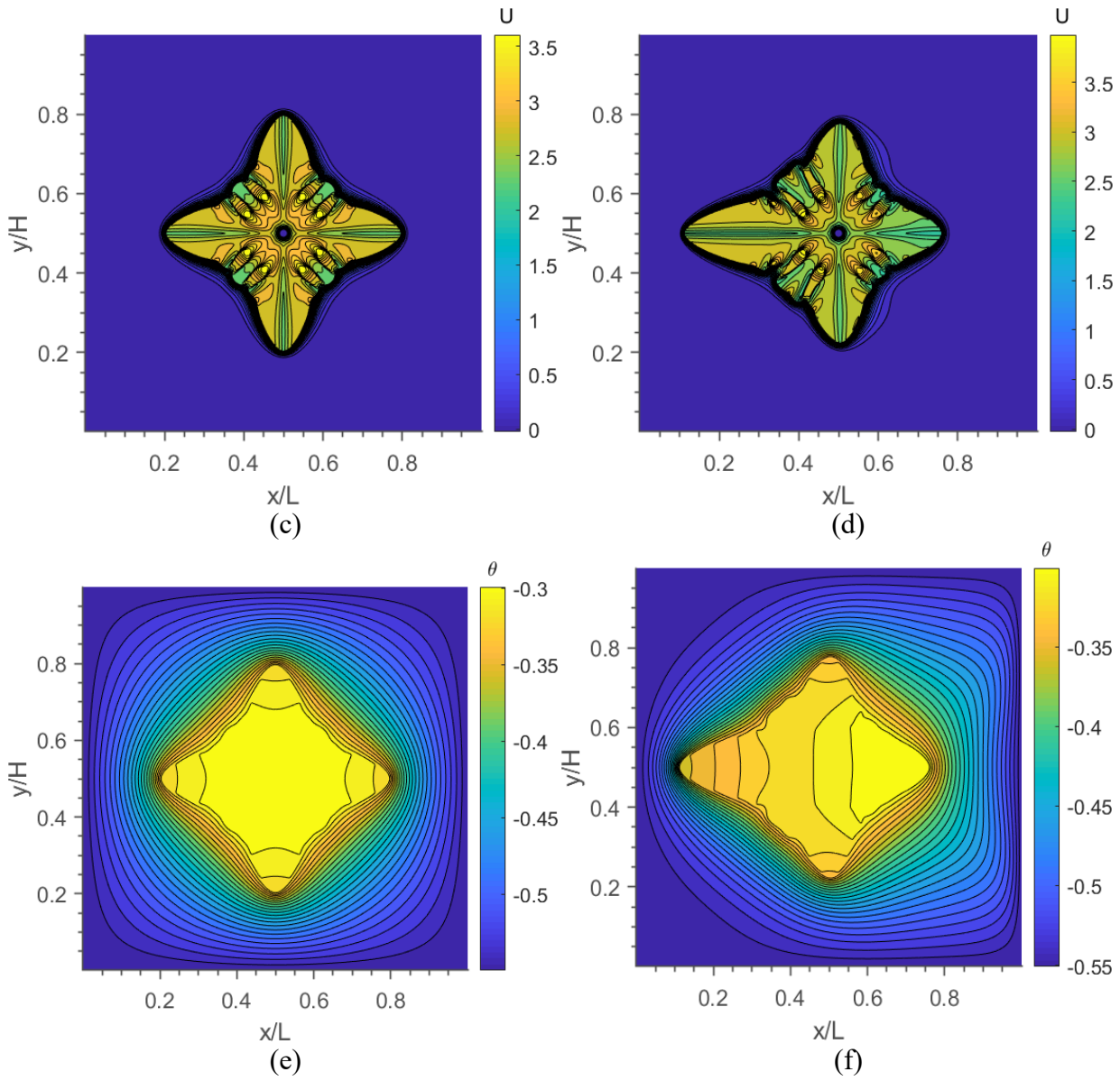

Fig. 16. Distributions of (a, b) the phase fields, (c, d) concentration fields, and (e, f) temperature fields at $tD_l / d_0^2 = 3500$ for the 2D fully coupled thermosolutal dendritic growth. (a, c, e) are simulations for the pure diffusion case and (b, d, f) for the convection-diffusion case both at *Le* = 50.

To further verify the temporal accuracy of the present model, Figs. 17 and 18 show the evolution of the primary tip velocity and tip radius results for the respective diffusion and convection-diffusion cases at *Le* = 50 and with the same parameters described above. The results from [1] are also included in Fig. 17 as references. First, the overall agreement in Fig. 17 is encouraging, especially for the excellent agreement of tip velocity at small times and the close

steady tip radius results. It should be noted that the present work represents the first quantitative comparison with the published data in [1] for the dendritic growth with coupled thermosolutal transport. Second, the present simulation results with two different R_s values confirm the sensitivity of the tip evolution with the initial seed size, which was also examined in detail in [37] in terms of interface morphology. Moreover, the results in Fig. 17 demonstrate that even though obvious discrepancies are noticed with different initial seed sizes, their steady-state (when domain size is large enough) results are almost identical for both tip velocity and radius. Compared to the large fluctuations in the data from [1] in Fig. 17 (a, b), it is believed that the present simulation results are more reliable. Lastly, the effect of the melt flow and convection on the evolution of the four primary tips is clearly seen in Fig. 18 (a, b). In summary, the present results in Figs. 17 and 18 can serve as benchmark data for verification of phase-field models for dendritic growth with fully coupled thermosolutal transport.

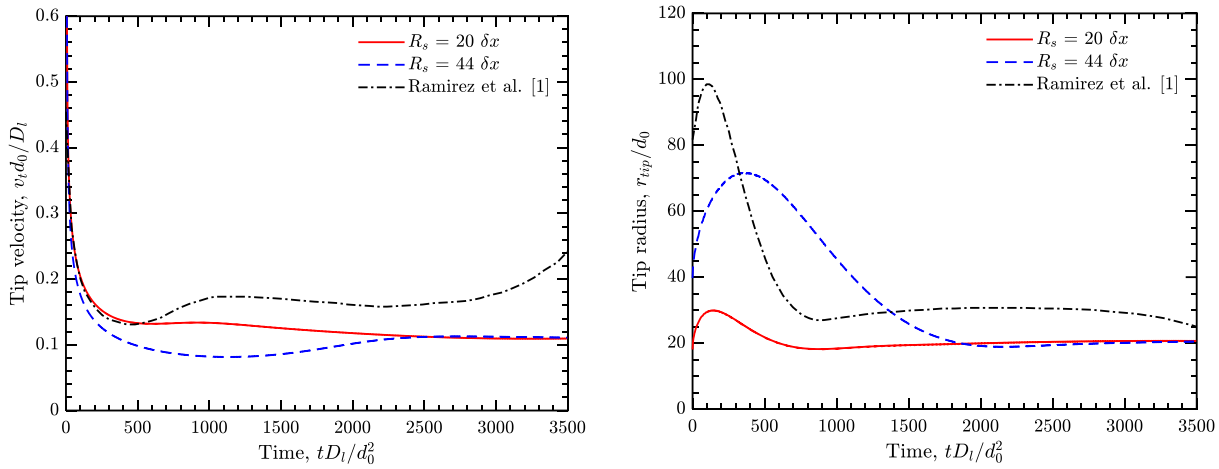

Fig. 17. Evolution of (a) the primary tip velocities and (b) tip radii for 2D dendritic growth with thermosolutal diffusion at *Le* = 50.

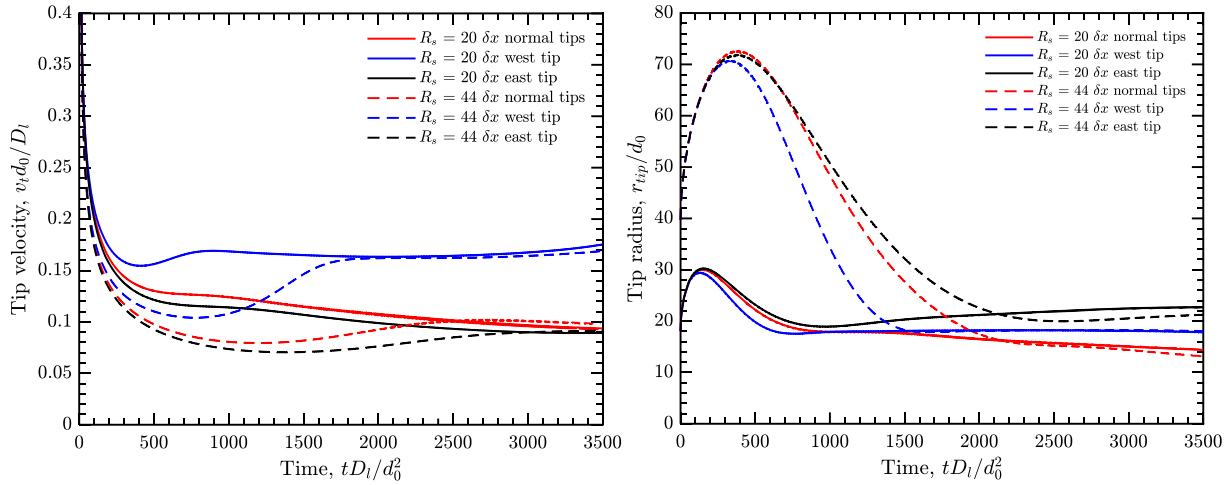

(a) (b)

Fig. 18. Evolution of (a) the primary tip velocities and (b) tip radii for the 2D dendritic growth with thermosolutal convection-diffusion at *Le* = 50.

4.4 Thermal/iso-solutal dendritic solidification in 3D

In this section, dendritic growth in 3D with pure diffusion is simulated to verify the present PFM/LBM model when extended to 3D. The thermal/iso-sloutal diffusion problem in Section 4.1 is directly extended to 3D with the same characteristic parameters $Le = 1$, $Mc_\infty = 0$, $\varepsilon_s = 0.05$ and $\lambda = 6.3826$. A computational domain with $385\delta x \times 385\delta x \times 385\delta x$ grid sizes and a spherical seed of initial radius $R_s = 10\delta x$ are used, and the interface thickness and reference time are selected as $W_0 = 2.5\delta x$ and $\tau_0 = 125\delta t$. Fig. 19 shows the representative phase-field and temperature distributions at $t/\tau_0 = 60$. The 3D contours in Fig. 19 (a, b) can be observed to be symmetric across the three central coordinate planes; and the 2D phase-field contours in Fig. 19 (c) are similar to those presented in Section 4.1. Furthermore, Fig. 20 compares the computed tip growth velocity and radius results with those reported by Jeong et al. [42], where excellent agreement for the tip velocities are observed in Fig. 20 (a), and similar trends in tip radii are shown in Fig. 20 (b) with slight discrepancies in magnitude. It should be noted that similar phenomena are observed and discussed in Section 4.3, the tip radius results are very sensitive to the initial seed size, the initial phase-field distribution and the evaluation schemes used.

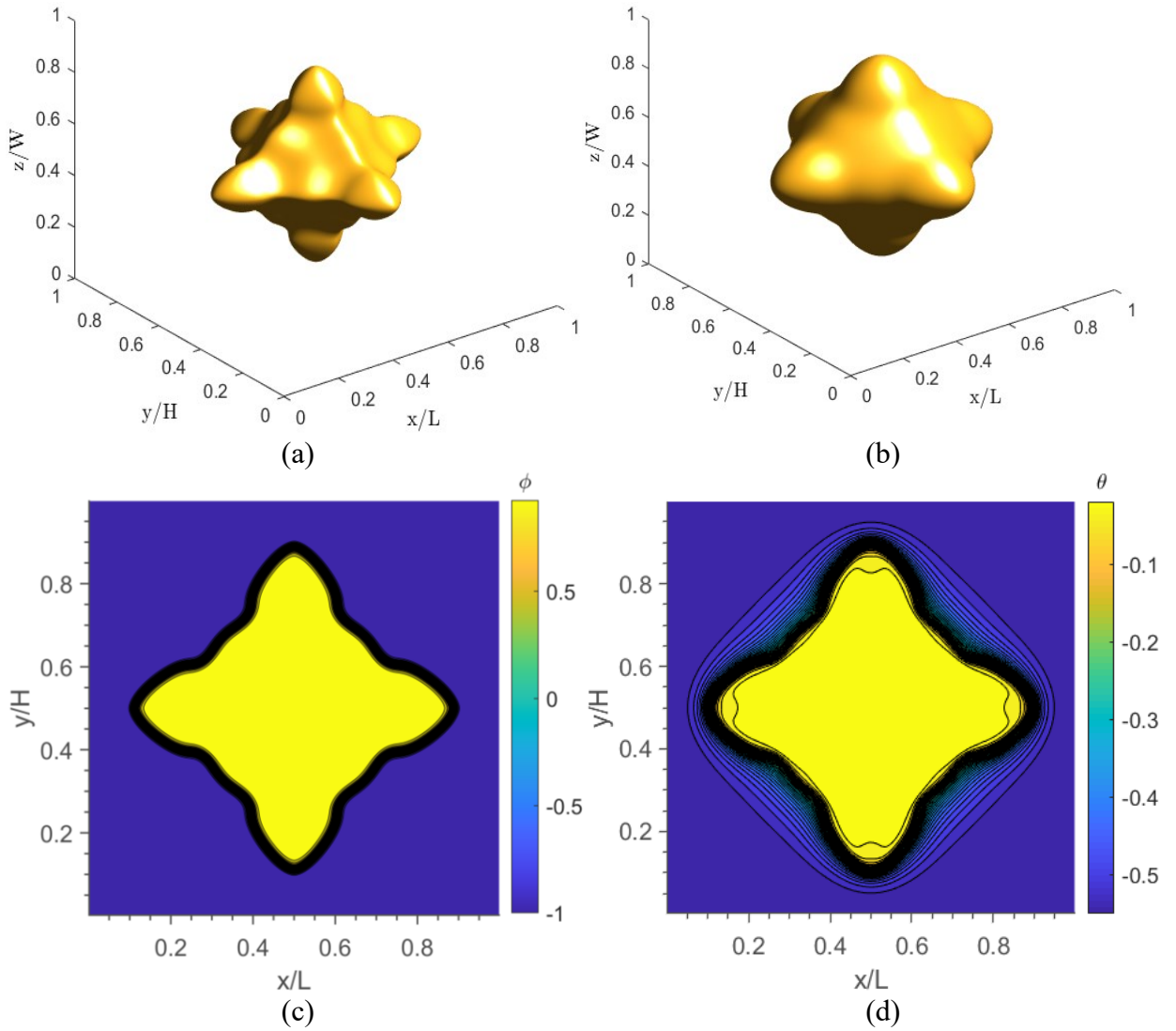

Fig. 19. (a) Dendritic shape at ϕ = 0 and (b) isothermal shape at θ = -0.25 in 3D, and (c) phase-field and (d) temperature contours in 2D on the central *x*-*y* plane for the 3D thermal/iso-solutal dendritic growth problem with pure diffusion. All results are at t/τ_0 = 60.

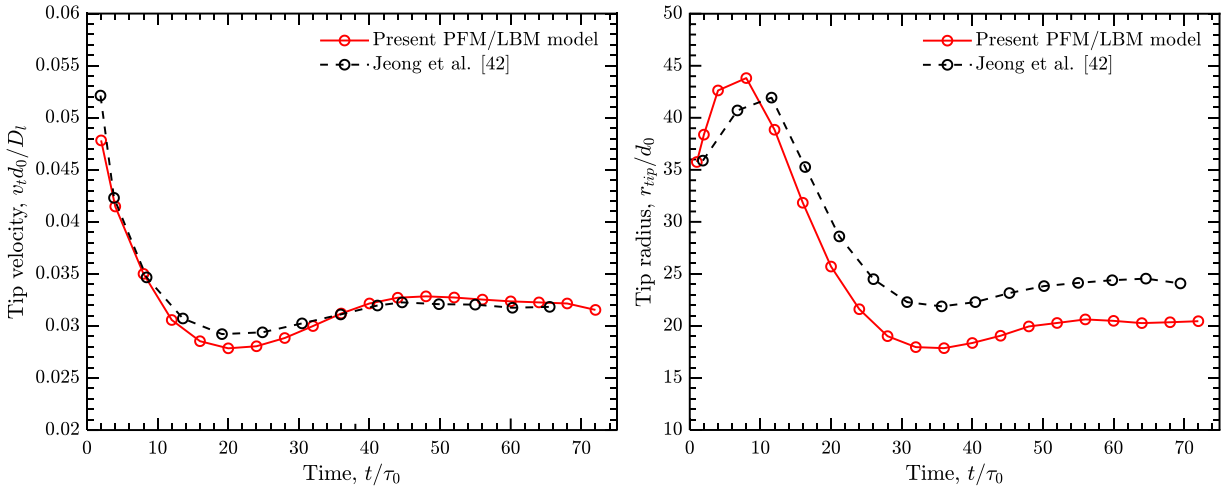

(a) (b)

Fig. 20. Evolution of (a) tip velocities and (b) tip radii on the central *x*-*y* plane for 3D dendritic growth with pure diffusion.

5. Conclusions

A new PFM/LBM model for solidification and dendritic growth simulation with fully coupled melt flow and thermosolutal convection-diffusion was developed in this work based on a synergy of the phase-field method (PFM) and the lattice Boltzmann method (LBM). The attractive feature of the diffuse interface in the PFM was maintained to effectively simulate the complex dendritic morphology evolution; and different from previous *hybrid* PFM-LBM models where the LBM was mainly applied to simulate the flow field, the present *coupled* PFM/LBM model inherits the intrinsic benefits of the LBM (e.g., simple and explicit algorithms, convenient boundary/interface treatment, and compatibility with parallelization), and all the evolution of the phase field, flow field, solute and thermal fields is simulated in the LB framework with a single Cartesian grid system. In addition, effective diffuse interface treatments are proposed in the LB schemes, which are directly implemented to the entire computational domain. Moreover, to improve the model stability and accuracy, multiple-relaxation-time (MRT) LB schemes are applied for all. Furthermore, in order to simulate various dendritic growth problems with wide ranges of characteristic parameters, a multiple-time-scaling strategy is employed in the LB framework that effectively decouples the times steps in the four LB schemes.

The efficacy of each of those unique features and the overall accuracy of the coupled PFM/LBM model were verified with representative numerical tests involving melt flow and thermosolutal convection-diffusion in 2D and pure diffusion in 3D. It was demonstrated that with

comparable spatial and temporal resolution, the present model showed more robust and consistent results than those in the literature in terms of the dendrite tip growth velocity and radius. The reported simulation results for thermosolutal dendritic solidification with and without convection can serve as reliable benchmark data.

Future studies will focus on applications of the verified PFM/LBM model to simulate large-scale dendritic growth such as those with natural and forced convection effects and involving dendrite motion driven by melt flow, and model validation with experimental measurements available in the literature.

Acknowledgements

This work was partially supported by the National Science Foundation (NSF award number OIA 2031701). The computer simulations used the NSF Extreme Science and Engineering Discovery Environment (XSEDE) under award allocation number TG-DMR190112 and the clusters in the High Performance Computing Collaboratory (HPC²) at Mississippi State University.

Appendix A. Chapman-Enskog Analysis of the MRT-LBM for the Phase-Field Equation

For the Chapman-Enskog expansion analysis, a "small" perturbation parameter ϵ, which is defined as the ratio of the lattice spacing δx to a characteristic macroscopic length L, i.e., $\epsilon \equiv \delta x / L$, is applied. The standard spatial scale $\mathbf{x}_1 = \epsilon\, \mathbf{x}$ and two time scales $t_1 = \epsilon\, t$ and $t_2 = \epsilon^2 t$ (hence $\nabla = \epsilon \nabla_1$, $\partial_t = \epsilon \partial_{t_1} + \epsilon^2 \partial_{t_2}$) are considered for the analysis, with also the following expansions introduced

$$g_\alpha = \sum_{n=0}^{\infty} \epsilon^n g_\alpha^{(n)}, \tag{A1}$$

$$g_\alpha \left(\mathbf{x} + \mathbf{e}_\alpha \delta t, t\right) = \sum_{n=0}^{\infty} \frac{\epsilon^n}{n!} \mathbf{d}^n g_\alpha^{(n)} \left(\mathbf{x}, t\right), \tag{A2a}$$

$$g_\alpha \left(\mathbf{x} + \mathbf{e}_\alpha \delta t, t + \delta t\right) = \sum_{n=0}^{\infty} \frac{\epsilon^n}{n!} \mathbf{D}^n g_\alpha^{(n)} \left(\mathbf{x}, t\right), \tag{A2b}$$

where $\mathbf{d} = \mathbf{e}_\alpha \cdot \nabla$, and $\mathbf{D} = \dfrac{\partial}{\partial t} + \mathbf{e}_\alpha \cdot \nabla$ is the convective derivative.

Following the similar steps in [31,43,48,52], one can insert the above expansions and rewrite the MRT-LB scheme in Eq. (19) in the consecutive orders of the parameter ϵ as follows

$$\mathrm{O}\left(\epsilon^0\right): \mathbf{\Lambda}_{\alpha\beta} \left[g_\beta^{(0)} - g_\beta^{\mathrm{eq}} \right] = 0, \tag{A3a}$$

$$\mathrm{O}\left(\epsilon^1\right): -\frac{1}{\delta t} \mathbf{\Lambda}_{\alpha\beta} g_\beta^{(1)} = \tilde{\mathbf{D}}_{1\alpha} g_\alpha^{(0)}, \tag{A3b}$$

$$\mathrm{O}\left(\epsilon^2\right): -\frac{1}{\delta t} \mathbf{\Lambda}_{\alpha\beta} g_\beta^{(2)} = a_s^2 \partial_{t_2} g_\alpha^{(0)} + \tilde{\mathbf{D}}_{1\alpha} g_\alpha^{(1)} + \frac{\delta t}{2} \tilde{\mathbf{D}}_{1\alpha}^2 g_\alpha^{(0)}, \tag{A3c}$$

where $\mathbf{\Lambda} \equiv \mathbf{M}^{-1}\mathbf{S}\mathbf{M}$ and $\tilde{\mathbf{D}}_{1\alpha} = a_s^2 \dfrac{\partial}{\partial t_1} + \mathbf{e}_\alpha \cdot \nabla_1$.

Since $\mathbf{\Lambda}$ is invertible, Eq. (A3a) simply implies

$$g_\alpha^{(0)} = g_\alpha^{\mathrm{eq}}. \tag{A4}$$

Also, the combination of Eqs. (A3b, A3c) gives

$$-\frac{1}{\delta t} \mathbf{\Lambda}_{\alpha\beta} g_\beta^{(2)} = a_s^2 \partial_{t_2} g_\alpha^{(0)} + \tilde{\mathbf{D}}_{1\alpha} \left(\mathbf{I} - \mathbf{\Lambda}/2\right)_{\alpha\beta} g_\beta^{(1)}. \tag{A5}$$

From the zeroth-order moments of $g_\alpha^{(1)}$ in Eq. (A3b) and $g_\alpha^{(2)}$ in Eq. (A5) one can obtain

$$a_s^2\partial_{t_1}\left(\sum_\alpha g_\alpha^{(0)}\right)+\nabla_1\cdot\left(\sum_\alpha \mathbf{e}_\alpha g_\alpha^{(0)}\right)=0, \tag{A6}$$

$$a_s^2\partial_{t_2}\left(\sum_\alpha g_\alpha^{(0)}\right)+\nabla_1\cdot\left[\left(\mathbf{I}-\mathbf{S}_1/2\right)_{\alpha\beta}\sum_\alpha \mathbf{e}_\alpha g_\alpha^{(1)}\right]=0, \tag{A7}$$

where the following relations are noted

$$\sum_\alpha \mathbf{c}_\alpha \mathbf{\Lambda}_{\alpha\beta}=s_0\mathbf{c}_\beta,\ \sum_\alpha \mathbf{e}_\alpha \mathbf{\Lambda}_{\alpha\beta}=\mathbf{S}_{10}\mathbf{c}_\beta+\mathbf{S}_1\mathbf{e}_\beta, \tag{A8}$$

with $\mathbf{c}=(1, 1, \ldots, 1)\in R^m$, s_0 a constant parameter, $\mathbf{S}_{10}$ a $m\times 1$ matrix, and $\mathbf{S}_1$ an invertible $m\times m$ relaxation matrix corresponding to the diffusion matrix [52].

Also from the first-order moment of $g_\alpha^{(1)}$ we obtain

$$\begin{aligned}\sum_\alpha \mathbf{e}_\alpha g_\alpha^{(1)} &= -\delta t\sum_\alpha \mathbf{e}_\alpha \mathbf{\Lambda}^{-1}_{\alpha\gamma}\tilde{\mathbf{D}}_{1\gamma}g_\gamma^{(0)} = -\delta t\mathbf{S}_1^{-1}\sum_\gamma \mathbf{e}_\gamma\tilde{\mathbf{D}}_{1\gamma}g_\gamma^{(0)}\\ &= -\delta t\mathbf{S}_1^{-1}\left[a_s^2\partial_{t_1}\left(\sum_\alpha \mathbf{e}_\alpha g_\alpha^{(0)}\right)+\nabla_1\cdot\sum_\alpha \mathbf{e}_\alpha\mathbf{e}_\alpha g_\alpha^{(0)}\right].\end{aligned} \tag{A9}$$

Eq. (A9) can be inserted into (A7) to yield

$$\begin{aligned}a_s^2\partial_{t_2}\left(\sum_\alpha g_\alpha^{(0)}\right) &= \delta t\nabla_1\cdot\left[\left(\mathbf{S}_1^{-1}-\mathbf{I}/2\right)\nabla_1\cdot\sum_\alpha \mathbf{e}_\alpha\mathbf{e}_\alpha g_\alpha^{(0)}\right]\\ &\quad+\delta t\nabla_1\cdot\left[\left(\mathbf{S}_1^{-1}-\mathbf{I}/2\right)a_s^2\partial_{t_1}\sum_\alpha \mathbf{e}_\alpha g_\alpha^{(0)}\right].\end{aligned} \tag{A10}$$

With the appropriate selection of $g_\alpha^{(0)}=g_\alpha^{\mathrm{eq}}$, $\partial_{t_1}\sum_\alpha \mathbf{e}_\alpha g_\alpha^{(0)}=0$ is noted and thus Eq. (A10) reduces to

$$a_s^2\partial_{t_2}\left(\sum_\alpha g_\alpha^{(0)}\right)=\delta t\nabla_1\cdot\left[\left(\mathbf{S}_1^{-1}-\mathbf{I}/2\right)\nabla_1\cdot\sum_\alpha \mathbf{e}_\alpha\mathbf{e}_\alpha g_\alpha^{(0)}\right]. \tag{A11}$$

Finally, we can combine the terms in $\epsilon\times$ Eq. (A6), $\epsilon^2\times$ Eq. (A11) and the source term of $O(\epsilon^2)$ to obtain

$$a_s^2\partial_t\left(\sum_\alpha g_\alpha^{(0)}\right)+\nabla\cdot\left(\sum_\alpha \mathbf{e}_\alpha g_\alpha^{(0)}\right)=\delta t\nabla\cdot\left[\left(\mathbf{S}_1^{-1}-\mathbf{I}/2\right)\nabla\cdot\sum_\alpha \mathbf{e}_\alpha\mathbf{e}_\alpha g_\alpha^{(0)}\right]+\delta t\sum_\alpha\frac{\omega_\alpha G_\phi}{F(U)\tau_0}. \tag{A12}$$

Clearly, with g_α^{eq} defined in Eq. (22), $\sum_\alpha g_\alpha^{(0)} = \phi$, $\sum_\alpha \mathbf{e}_\alpha g_\alpha^{(0)} = -\mathbf{N}\frac{W_0^2}{F(U)\tau_0}\frac{\delta t}{\delta x}$ and $\sum_\alpha \mathbf{e}_\alpha \mathbf{e}_\alpha g_\alpha^{(0)} = \xi\phi\mathbf{I}$ can be readily verified; also, recalling the relaxation matrix in Eq. (23), Eq. (A12) becomes

$$a_s^2 \partial_t \phi = \nabla \cdot \left[\frac{a_s^2}{F(U)} \frac{W_0^2}{\tau_0} \nabla \phi \right] + \frac{W_0^2}{\tau_0} \nabla \cdot \frac{\mathbf{N}}{F(U)} + \frac{G_\phi}{F(U)\tau_0} . \tag{A13}$$

Eq. (A13) is identical to the governing equation in (18) when preserving the terms up to $\mathrm{O}\left(\epsilon^2\right)$. It is thus verified that the MRT-LB evolution scheme in Eq. (19) recovers the governing equation for the phase field up to second-order accuracy.

Appendix B. Evaluation of the Tip Velocity and Radius

With the objective of accurately evaluating the tip velocity and tip radius during the dendritic growth, bi-cubic interpolation using 16 data points of the phase field variable, ϕ_{ij}, ($i = 1 \sim 4, j = 1 \sim 4$) enclosing each tip is applied. Through the introduction of a local coordinate system (ξ, η), the bi-cubic function is constructed as $\phi(\xi,\eta) = \sum_{\alpha=0}^{3}\sum_{\beta=0}^{3} C_{\alpha\beta}\xi^{\alpha}\eta^{\beta}$ where $C_{\alpha\beta}$ are constant coefficients that can be easily determined with the ϕ_{ij} values from the phase-field solution.

In addition, the Newton-Raphson method for root-finding in 2D is employed to accurately determine the tip coordinates (ξ_t, η_t) that satisfy the two conditions of $\phi(\xi_t,\eta_t) = 0$, and $\frac{\partial\phi}{\partial\xi}\Big|_{(\xi_t,\eta_t)} = 0$ (for north and south tips) or $\frac{\partial\phi}{\partial\eta}\Big|_{(\xi_t,\eta_t)} = 0$ (for west and east tips). After determining the tip coordinates, the tip velocity can be readily calculated in the time marching procedure, and the tip radius is analytically calculated according to $\rho_{\text{tip}} = \frac{\partial_\eta\phi\big|_{(\xi_t,\eta_t)}}{\partial^2_\xi\phi\big|_{(\xi_t,\eta_t)}}$ (for north and south tips) and $\rho_{\text{tip}} = \frac{\partial_\xi\phi\big|_{(\xi_t,\eta_t)}}{\partial^2_\eta\phi\big|_{(\xi_t,\eta_t)}}$ (for west and east tips).

For 3D simulations, the center of the initial spherical seed is placed exactly on a lattice node, and the tip velocity and radius are evaluated on the selected 2D planes following the same process described above.

References

[1] J.C. Ramirez, C. Beckermann, A. Karma, H.J. Diepers, Phase-field modeling of binary alloy solidification with coupled heat and solute diffusion, Phys. Rev. E - Stat. Physics, Plasmas, Fluids, Relat. Interdiscip. Top. 69 (2004) 16. doi:10.1103/PhysRevE.69.051607.

[2] W.J. Boettinger, J.A. Warren, C. Beckermann, A. Karma, PHASE-FIELD SIMULATION OF SOLIDIFICATION 1, Annu. Rev. Mater. Res. 32 (2002) 163–94. doi:10.1146/annurev.matsci.32.101901.155803.

[3] M. Asta, C. Beckermann, A. Karma, W. Kurz, R. Napolitano, M. Plapp, G. Purdy, M. Rappaz, R. Trivedi, Solidification microstructures and solid-state parallels: Recent developments, future directions, Acta Mater. 57 (2009) 941–971. doi:10.1016/j.actamat.2008.10.020.

[4] I. Steinbach, Why Solidification? Why Phase-Field?, (n.d.). doi:10.1007/s11837-013-0681-5.

[5] L.-Q. Chen, PHASE-FIELD MODELS FOR MICROSTRUCTURE EVOLUTION, Annu. Rev. Mater. Res. 32 (2002) 113–153. doi:10.1146/annurev.matsci.32.112001.132041.

[6] N. Valizadeh, T. Rabczuk, Isogeometric analysis for phase-field models of geometric PDEs and high-order PDEs on stationary and evolving surfaces, Comput. Methods Appl. Mech. Eng. 351 (2019) 599–642. doi:10.1016/j.cma.2019.03.043.

[7] D. Medina, N. Valizadeh, E. Samaniego, A.X. Jerves, T. Rabczuk, Isogeometric analysis of insoluble surfactant spreading on a thin film, Comput. Methods Appl. Mech. Eng. 370 (2020) 113272. doi:10.1016/j.cma.2020.113272.

[8] M. Ashour, N. Valizadeh, T. Rabczuk, Isogeometric analysis for a phase-field constrained optimization problem of morphological evolution of vesicles in electrical fields, Comput. Methods Appl. Mech. Eng. 377 (2021) 113669. doi:10.1016/j.cma.2021.113669.

[9] S.R. Coriell, W.J. Boettinger, M.R. Cordes, R.F. Sekerka, Effect of gravity on coupled convective and interfacial instabilities during directional solidification, Adv. Sp. Res. (1981). doi:10.1016/0273-1177(81)90142-3.

[10] S.H. Davis, Hydrodynamic interactions in directional solidification, J. Fluid Mech. (1990). doi:10.1017/S002211209000194X.

[11] R. Ananth, W.N. Gill, Dendritic growth of an elliptical paraboloid with forced convection in the melt, J. Fluid Mech. (1989). doi:10.1017/S0022112089002946.

[12] J.J. Xu, Dendritic Growth from a Melt in an External Flow: Uniformly Valid Asymptotic Solution for the Steady State, J. Fluid Mech. (1994). doi:10.1017/S002211209400409X.

[13] C. Beckermann, H.-J. Diepers, I. Steinbach, A. Karma, X. Tong, Modeling Melt Convection in Phase-Field Simulations of Solidification, J. Comput. Phys. 154 (1999) 468–496. doi:10.1006/JCPH.1999.6323.

[14] D. Medvedev, K. Kassner, Lattice Boltzmann scheme for crystal growth in external flows, (n.d.). doi:10.1103/PhysRevE.72.056703.

[15] L. Yuan, P.D. Lee, Dendritic solidification under natural and forced convection in binary alloys: 2D versus 3D simulation, Model. Simul. Mater. Sci. Eng. 18 (2010). doi:10.1088/0965-0393/18/5/055008.

[16] T. Takaki, Phase-field Modeling and Simulations of Dendrite Growth, ISIJ Int. 54 (2014) 437–444. doi:10.2355/isijinternational.54.437.

[17] R. Rojas, T. Takaki, M. Ohno, A phase-field-lattice Boltzmann method for modeling motion and growth of a dendrite for binary alloy solidification in the presence of melt convection, J. Comput. Phys. 298 (2015) 29–40. doi:10.1016/j.jcp.2015.05.045.

[18] T.Z. Gong, Y. Chen, D.Z. Li, Y.F. Cao, P.X. Fu, Quantitative comparison of dendritic growth under forced flow between 2D and 3D phase-field simulation, Int. J. Heat Mass Transf. 135 (2019) 262–273. doi:10.1016/j.ijheatmasstransfer.2019.01.104.
[19] R. Benzi, S. Succi, M. Vergassola, The lattice Boltzmann equation: theory and applications, Phys. Rep. (1992). doi:10.1016/0370-1573(92)90090-M.
[20] X. He, L.S. Luo, Lattice Boltzmann model for the incompressible Navier-Stokes equation, J. Stat. Phys. (1997). doi:10.1023/b:joss.0000015179.12689.e4.
[21] S. Chen, G.D. Doolen, Lattice Boltzmann Method for Fluid Flows, Annu. Rev. Fluid Mech. 30 (2002) 329–364. doi:10.1146/annurev.fluid.30.1.329.
[22] D. Yu, R. Mei, L.S. Luo, W. Shyy, Viscous flow computations with the method of lattice Boltzmann equation, Prog. Aerosp. Sci. 39 (2003) 329–367. doi:10.1016/S0376-0421(03)00003-4.
[23] C.K. Aidun, J.R. Clausen, Lattice-Boltzmann Method for Complex Flows, Annu. Rev. Fluid Mech. 42 (2009) 439–472. doi:10.1146/annurev-fluid-121108-145519.
[24] H. Yoshida, M. Nagaoka, Multiple-relaxation-time lattice Boltzmann model for the convection and anisotropic diffusion equation, J. Comput. Phys. 229 (2010) 7774–7795. doi:10.1016/j.jcp.2010.06.037.
[25] L. Li, R. Mei, J.F. Klausner, Boundary conditions for thermal lattice Boltzmann equation method, J. Comput. Phys. 237 (2013) 366–395. doi:10.1016/j.jcp.2012.11.027.
[26] L. Li, C. Chen, R. Mei, J.F. Klausner, Conjugate heat and mass transfer in the lattice Boltzmann equation method, Phys. Rev. E. 89 (2014). doi:10.1103/PhysRevE.89.043308.
[27] L. Li, R. Mei, J.F. Klausner, Lattice Boltzmann models for the convection-diffusion equation: D2Q5 vs D2Q9, Int. J. Heat Mass Transf. 108 (2017) 41–62. doi:10.1016/j.ijheatmasstransfer.2016.11.092.
[28] T. Takaki, R. Rojas, S. Sakane, M. Ohno, Y. Shibuta, T. Shimokawabe, T. Aoki, Phase-field-lattice Boltzmann studies for dendritic growth with natural convection, J. Cryst. Growth. 474 (2017) 146–153. doi:10.1016/j.jcrysgro.2016.11.099.
[29] T. Takaki, S. Sakane, M. Ohno, Y. Shibuta, T. Aoki, Large–scale phase–field lattice Boltzmann study on the effects of natural convection on dendrite morphology formed during directional solidification of a binary alloy, Comput. Mater. Sci. 171 (2020) 109209. doi:10.1016/J.COMMATSCI.2019.109209.
[30] Z. Guo, J. Mi, S. Xiong, P.S. Grant, Phase field study of the tip operating state of a freely growing dendrite against convection using a novel parallel multigrid approach, J. Comput. Phys. 257 (2014) 278–297. doi:10.1016/j.jcp.2013.10.004.
[31] A. Cartalade, A. Younsi, M. Plapp, Lattice Boltzmann simulations of 3D crystal growth: Numerical schemes for a phase-field model with anti-trapping current, Comput. Math. with Appl. 71 (2016) 1784–1798. doi:10.1016/j.camwa.2016.02.029.
[32] A. Younsi, A. Cartalade, On anisotropy function in crystal growth simulations using Lattice Boltzmann equation, J. Comput. Phys. 325 (2016) 1–21. doi:10.1016/j.jcp.2016.08.014.
[33] D. Sun, H. Xing, X. Dong, Y. Han, An anisotropic lattice Boltzmann – Phase field scheme for numerical simulations of dendritic growth with melt convection, Int. J. Heat Mass Transf. 133 (2019) 1240–1250. doi:10.1016/j.ijheatmasstransfer.2018.12.095.
[34] X. Wang, D. Sun, H. Xing, Y. Han, Y. Liu, J. Wang, Numerical modeling of equiaxed crystal growth in solidification of binary alloys using a lattice Boltzmann-finite volume scheme, Comput. Mater. Sci. 184 (2020) 109855. doi:10.1016/j.commatsci.2020.109855.
[35] L. Rátkai, T. Pusztai, L. Gránásy, Phase-field lattice Boltzmann model for dendrites

growing and moving in melt flow, Npj Comput. Mater. 5 (2019). doi:10.1038/s41524-019-0250-8.
[36] A. Karma, Phase-field formulation for quantitative modeling of alloy solidification, Phys. Rev. Lett. (2001). doi:10.1103/PhysRevLett.87.115701.
[37] Z. Guo, J. Mi, P.S. Grant, An implicit parallel multigrid computing scheme to solve coupled thermal-solute phase-field equations for dendrite evolution, J. Comput. Phys. 231 (2012) 1781–1796. doi:10.1016/j.jcp.2011.11.006.
[38] Z. Guo, S.M. Xiong, On solving the 3-D phase field equations by employing a parallel-adaptive mesh refinement (Para-AMR) algorithm, Comput. Phys. Commun. 190 (2015) 89–97. doi:10.1016/j.cpc.2015.01.016.
[39] A. Zhang, J. Du, J. Yang, Z. Guo, Q. Wang, B. Jiang, F. Pan, S. Xiong, General hierarchical structure to solve transport phenomena with dissimilar time scales: Application in large-scale three-dimensional thermosolutal phase-field problems, Phys. Rev. E. 102 (2020) 43313. doi:10.1103/PhysRevE.102.043313.
[40] L. Li, Multiple-time-scaling lattice Boltzmann method for the convection diffusion equation, Phys. Rev. E. 99 (2019) 1–13. doi:10.1103/PhysRevE.99.063301.
[41] S. Meng, A. Zhang, Z. Guo, Q. Wang, Phase-field-lattice Boltzmann simulation of dendrite motion using an immersed boundary method, Comput. Mater. Sci. 184 (2020) 109784. doi:10.1016/j.commatsci.2020.109784.
[42] J.H. Jeong, N. Goldenfeld, J.A. Dantzig, Phase field model for three-dimensional dendritic growth with fluid flow, Phys. Rev. E - Stat. Physics, Plasmas, Fluids, Relat. Interdiscip. Top. (2001). doi:10.1103/PhysRevE.64.041602.
[43] S.D.C. Walsh, M.O. Saar, Macroscale lattice-Boltzmann methods for low Peclet number solute and heat transport in heterogeneous porous media, Water Resour. Res. 46 (2010). doi:10.1029/2009WR007895.
[44] P.L. Bhatnagarp, E.P. Gross, A.M. Krook, A Model for Collision Processes in Gases. I. Small Amplitude Processes in Charged and Neutral One-Component Systems, Phys. Rev. 94 (1954) 511–525.
[45] I. D'Humieres, Dominique Ginzburg, M. Krafczyk, P. Lallemand, L.-S. Luo, Multiple-relaxation-time lattice Boltzmann models in three dimensions, Philos. Trans. A. Math. Phys. Eng. Sci. 360 (2011) 437–451.
[46] P. Lallemand, L.-S. Luo, Theory of the lattice Boltzmann method: Dispersion, dissipation, isotropy, Galilean invariance, and stability, Phys. Rev. E. 61 (2000) 6546–6562. doi:10.1103/PhysRevE.61.6546.
[47] L. Li, R. Mei, J.F. Klausner, Heat Transfer Evaluation on Curved Boundaries in Thermal Lattice Boltzmann Equation Method, J. Heat Transfer. 136 (2014) 012403. doi:10.1115/1.4025046.
[48] C. Chen, L. Li, R. Mei, J.F. Klausner, Chapman–Enskog Analyses on the Gray Lattice Boltzmann Equation Method for Fluid Flow in Porous Media, J. Stat. Phys. 171 (2018) 493–520. doi:10.1007/s10955-018-2005-1.
[49] H. Yoshida, H. Hayashi, Transmission-Reflection Coefficient in the Lattice Boltzmann Method, J. Stat. Phys. 155 (2014) 277–299. doi:10.1007/s10955-014-0953-7.
[50] I. Ginzburg, Comment on "An improved gray Lattice Boltzmann model for simulating fluid flow in multi-scale porous media": Intrinsic links between LBE Brinkman schemes, Adv. Water Resour. 88 (2016) 241–249. doi:10.1016/j.advwatres.2014.05.007.
[51] S. Sakane, T. Takaki, M. Ohno, Y. Shibuta, T. Aoki, Two-dimensional large-scale phase-

field lattice Boltzmann simulation of polycrystalline equiaxed solidification with motion of a massive number of dendrites, Comput. Mater. Sci. 178 (2020) 109639. doi:10.1016/j.commatsci.2020.109639.
[52] Z. Chai, B. Shi, Multiple-relaxation-time lattice Boltzmann method for the Navier-Stokes and nonlinear convection-diffusion equations: Modeling, analysis, and elements, Phys. Rev. E. 102 (2020). doi:10.1103/PhysRevE.102.023306.